NTNU – Trondheim
Norwegian University of
Science and Technology

Investigation of Routes for Improving the Rate Capability of Electrodes in Li-ion Batteries

Marita Sætnan

Chemical Engineering and Biotechnology
Submission date: June 2014
Supervisor: Ann Mari Svensson, IMTE
Co-supervisor: Ahmet Oguz Tezel, IMTE

Norwegian University of Science and Technology
Department of Materials Science and Engineering

Problem description

Batteries and supercapacitors are important energy storage technologies, and are receiving increasing attention due to the developments in the transportation sector, with hybrid and all-electric vehicles, as well as for storage of energy from renewable sources. In particular the development of Li-ion batteries has paved the way for consumer electronics, and is also the dominating battery technology for transportation, due to the high energy density. Still, there are many challenges associated with the Li-ion technology. These include life-time and degradation, cost, safety, as well as energy and power density. The latter is important for optimal performance of the batteries both in vehicles (acceleration) and for storage from renewables.

There are several factors that influence the rate capability of Li-ion batteries. For the electrodes, in particular the cathode, good electronic network, high Li-ion diffusion rates in the solid and good transport properties of Li-ions in the electrolyte is crucial. For the anode, a lowest possible resistance of the solid electrolyte interface (SEI layer) is important in addition. The objective of this work is to investigate routes for improving the rate capability of anodes and cathodes in Li-ion batteries. These include improving the electronically conducting network of the electrodes by reducing the interfacial contact resistivity to the current collector, replacing the carbon black conductive additive by graphite/graphene, as well as reducing the resistance related to intercalation of Li into the graphite particles by modifying the electrolyte.

Declaration

I hereby declare that this work has been performed independently and in accordance with the rules and regulations for examinations at the Norwegian University of Science and Technology (NTNU).

Trondheim, June 16, 2014

Marita Sætnan

Preface

This thesis presents the work carried out at the Department of Materials Science and Engineering at the Norwegian University of Science and Technology (NTNU) during the spring semester, 2014. This work is a part of the battery research in the Electrochemical Energy Research Group at NTNU. The aim of this thesis was to investigate ways to improve the rate capability of electrodes for use in lithium-ion batteries.

Most experiments and analyses described in this thesis were conducted at the Department of Materials Science and Engineering at NTNU by the author. Some electrolyte preparations were made in collaboration with another master student, Benedicte Eikeland Nilssen, as we used the same electrolytes in our work.

First of all, I would like to thank my main supervisor, Professor Ann Mari Svensson, for always being supportive and helpful. She has shown commitment to my work and she has always been available when needed. I have appreciated our weekly meetings and her guidance and feedback have been invaluable. Further, I would like to thank my co-supervisor PhD Fellow Ahmet Oguz Tezel for informal discussions, literature recommendations and lab advice.

In addition, I want to thank Senior Engineer Yingda Yu for training and guidance on the SEM, Head Engineer at NTNU NanoLab Espen Rogstad for training and assistance on the Thermal CVD work and PhD Fellow Andrey Sergeevich Volynkin for instruction on the Raman spectroscope. They have all been very accommodating and helpful.

Further I would like to thank Erlend Kvinge Jørgensen for help with encoding `KalmanFilt_h.m` and Øyvind Ulvin Halvorsen for invaluable help with MATLAB throughout the semester.

Finally, I would like to thank my fellow student, Benedicte Eikeland Nilssen, for assistance in the understanding of the basics concepts I needed to learn when I started as a new masters student within this field in January. She is always positive and her constant eagerness to learn more has been very inspiring.

Abstract

Lithium-ion battery, first introduced to market in 1991 by Sony, is today one of the most popular battery technologies in the world. The development of Li-ion battery applications from portable electronic devices to electric vehicles and energy storages system has resulted in escalating demand for high-power performance of the batteries.

In this thesis, various methods to improve the rate capability of Li-ion electrodes were investigated. These include improving the electronically conducting network of the electrodes by reducing the interfacial contact resistivity to the current collector, replacing the carbon black conductive additive by graphite/graphene, as well as reducing the resistance related to intercalation of lithium-ions into the graphite particles by addition of anion receptor in the electrolyte. In order to reduce the interfacial resistance between the current collector and the active electrode material, a carbon layer was deposited onto current collectors by thermal chemical vapor deposition before electrode casting. Li-ion half-cell batteries were manufactured and cycled at different rates in order to reveal the electrochemical performance. Characterizations of the materials were conducted, among them scanning electron microscopy investigations and Raman spectroscopy measurements.

It was found, based on average capacity values, that cells with carbon coated current collector demonstrated higher capacities and improved rate capabilities compared to cells without coating. However, there were considerable individual differences among the various cells and hence, more parallel experiments should be performed in order to understand the effect of the coating. Based on average capacity values, addition of anion receptor in the electrolyte also resulted in higher capacities and improved rate capabilities. Additionally, differential capacity data indicated that overpotential associated with SEI formation on the anode in the first cycle was reduced with presence of anion receptor in the electrolyte and that overpotentials associated with intercalation and de-intercalation was lowered.

For the cathode cells, replacement of carbon black by graphene nanopowder did not improve the cell performance. By comparing the particle size of the various materials it was clear that the graphene material, graphene nanopow-

der, would be less able to create a continuous conductive network throughout the electrode. Raman measurements also showed that the graphene nanopowder was not perfect graphene, but likely somewhat more similar to graphite.

Sammendrag

Litium-ion batteriet, først introdusert i 1991 av Sony, er i dag en av de mest populære batteriteknologiene i verden. Utviklingen av bruksområder for Li-ion batterier de senere årene, fra bruk i bærbare elektriske apparater til kraftforsyning av elektriske biler, har gjort at behovet for batterier med høy strømytelse har eskalert.

I denne masteroppgaven har ulike metoder for å bedre rate kapabiliteten til Li-ion elektroder blitt undersøkt. Disse metodene inkluderer forbedring av elektronisk ledende nettverk i elektrodene ved reduksjon av grenseflatemotstand til strømsamler, erstatning av carbon black med grafitt/grafen som ledende additiv i katoden, samt tilsetting av anion-reseptor i elektrolytt for reduksjon av motstand i forbindelse med interkalering av litium-ioner inn i grafittpartikler. I forsøket på å redusere grenseflatemotstand til strømsamler ble et karbon-lag deponert på strømsamleren ved termo-kjemisk dampdeponering før elektrodematerialet ble avstøpt. Halvcelle Li-ion batterier ble satt sammen og syklet med ulike hastigheter for å avdekke den elektrokjemiske ytelsen. Materialkarakterisering ble gjennomført ved hjelp av sveipeelektronmikroskopi og Raman spektroskopi.

Det ble funnet at deponeringen av et karbon-lag på overflaten av strømsamleren i snitt gav bedre kapasitetsverdier, men at det var betydelige individuelle forskjeller blant de ulike cellene. Tilsetting av anion-reseptor i elektrolytt gav også i snitt bedre kapasitetsverdier. Videre indikerte utvalgte differensielle kapasitetsverdier at overpotensial forbundet med SEI dannelse på anodeoverflaten i første sykel ble redusert ved tilstedeværelse av anion-reseptor i elektrolytten, og at anion-reseptor bidro til reduksjon av overpotensialer i cellen relatert til interkalering og de-interkalering.

For katodecellene ble det funnet at erstatning av carbon black med grafitt/-grafen ikke forbedret celle ytelsen. Ved sammenligning av partikkelstørrelser for de ulike materialene kommer det klart frem at grafen-materialet som er brukt, graphene nanopowder, vil være mindre i stand til å skape et kontinuerlig ledende nettverk i elektroden enn carbon black. Raman målinger viste også at graphene nanopowder ikke var perfekt grafen, men sannsynligvis noe mer lik grafitt i struktur.

List of Figures

List of Tables

List of Abbreviations

BET Brunauer-Emmett-Teller (specific surface area measurement method)

BSE Backscattered electrons

CVD Chemical vapor deposition

DEC Diethyl carbonate

DMC Dimethyl carbonate

EBSD Diffracted backscattered electrons

EC Ethylene carbonate

EMC Ethylmethyl carbonate

GIC Graphite intercalation compounds

HOMO Highest occupied molecular orbital

ICL Irreversible capacity loss

LUMO Lowest unoccupied molecular orbital

NMP 1-methyl-2-pyrrolidinone

PC Propylene carbonate

PVDF Polyvinylidene fluoride

SE Secondary electrons

SEI Solid electrolyte interface

SEM Scanning electron microscopy

THFIPB Tris(hexafluoroisopropyl) borate

TPFPB Tris(pentafluorophenyl) borane

Contents

1. Introduction

1.1 Motivation

The energy economy of today is mainly based on fossil fuels and is at serious risk due to numerous factors. These factors include the continuous increase in the demand for oil, excessive extraction of non-renewable sources resulting in depletion of reservoirs and political instabilities in oil-producing countries. In addition, CO_2 emissions are a worrying aspect of the fossil fuel energy economy, as the CO_2 level has almost doubled from 1970 to 2005. The consequence is a rise in global temperature with associated series of dramatic climate changes. Issues related to CO_2 emissions may be solved by replacing internal combustion engine (ICE) vehicles with ideally zero emission or controlled emission vehicles, e.g. electric vehicles (EVs) or full hybrid electric vehicles (HEVs) [1].

New energy technologies are vital for the realization of a sustainable energy future. The lithium-ion battery, first introduced to market in 1991 by Sony, is today one of the most popular battery technologies in the world [2]. For use in portable electronic devices lithium-ion batteries are currently the systems of choice, providing high gravimetric and volumetric energy densities, flexible and lightweight design, and longer lifespan than comparable battery technologies [3]. Figure 1.1 illustrates a comparison of different battery technologies in terms of volumetric and gravimetric energy density. The recent development of Li-ion battery applications from portable electronic devices to electric vehicles and energy storages system has resulted in escalating demand for high-power performance of these batteries [2].

In practice, it is hard to meet numerous battery performance requirements simultaneously. High specific energy, high rate capability, long life, low cost, perfect safety, and minimal environmental impact are all desired characteristics of batteries. Lithium-ion batteries have the potential to be "the battery of choice" for HEVs compared to other batteries, but unfortunately, successful application is limited by low rate capability, high cost, and issues regarding safety performance [4].

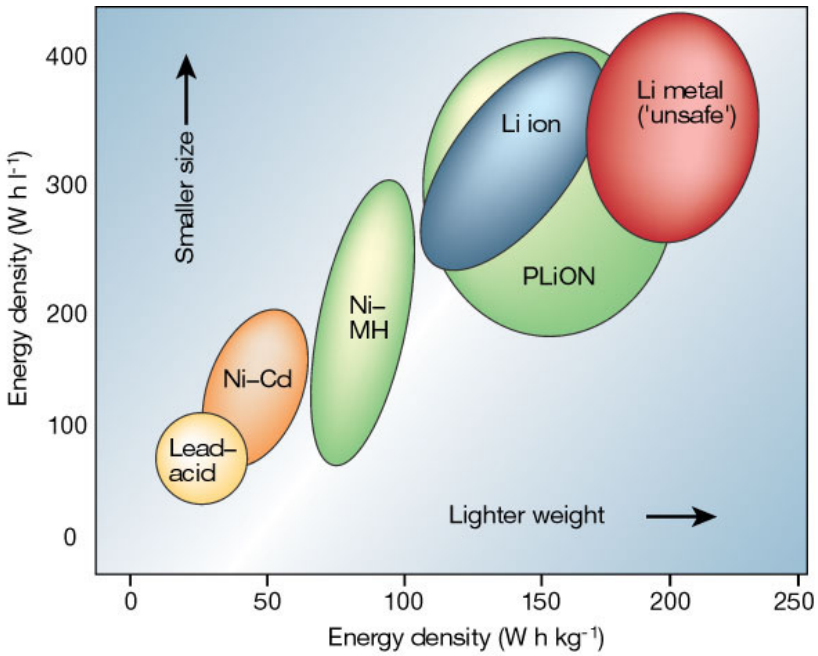

Figure 1.1: A comparison of volumetric and gravimetric energy densities for different battery technologies. Modified from [3].

1.2 Aim of this work

This thesis aims to investigate ways to improve the rate capability of anodes and cathodes in Li-ion batteries. The main focus of this study has been on the negative electrode. The studies of the anode include improvement of the electrically conducting network of the electrode by reducing the interfacial contact resistivity to the current collector as well as reduction of the resistance related to lithium intercalation into the graphite particles by modifying the electrolyte. For the positive electrode this involves improvement of the electronically conducting network of the electrodes by replacing the carbon black conductive additive by graphite/graphene.

2. Theory

2.1 Electrochemical principles of lithium-ion battery cells

The main principle behind battery operation is that chemical energy stored in the active materials of the battery is converted into electrical energy by an electrochemical oxidation-reduction (redox) reaction. Such reactions involve the transfer of electrons from one material to another by an outer circuit. So-called secondary batteries are rechargeable, meaning that electrode reactions may be reversed.

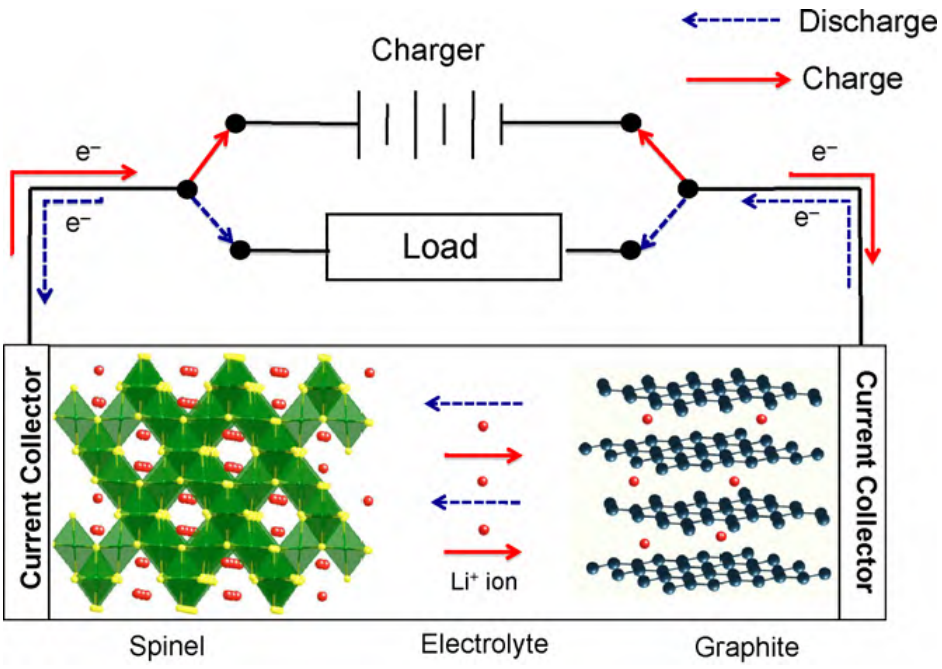

Figure 2.1: Operating principles of a lithium-ion cell. Upon discharge, the negative electrode (the graphite electrode) undergoes an oxidation and the positive electrode (the spinel structured electrode) sees a reduction. The movement of charges is reversed upon charging [5].

A battery consists of one or more electrochemical units, called cells, which are coupled in parallel or series or both in order to achieve the desired voltage and/or capacity. An illustration of the operating principle of a Li-ion battery cell is shown in Figure 2.1. Battery cells consists of three major components [6]:

1. The negative electrode: the electrode that gives up electrons to the outer circuit and is oxidized during the discharge reaction (and reduced during charging).
2. The positive electrode: the electrode that receives electrons from the outer circuit and is reduced during the discharge reaction (and oxidized during charging).
3. The electrolyte: the medium that enables transfer of ions between the electrodes inside the cell.

Inside the battery, the two electrodes are electronically separated to avoid internal short-circuit. This means in practice, that a separator material is placed between the anode and cathode. A porous separator i normally used to fix the electrolyte between the electrodes, and prevent short circuiting. The key property of separator materials is that they are permeable to the electrolyte, in order to maintain the required ionic conductivity.

2.2 The electrode reactions and intercalation processes

During operation of secondary Li-ion batteries, lithium-ions migrate back and forth through the electrolyte and intercalate the electrodes. Upon charging, lithium-ions originating from the positive electrode host structure (a lithium metal oxide) move through the electrolyte and are reversibly inserted into the negative electrode host structure (a carbon structure). The direction of lithium migration is reversed upon discharge. The electrochemical reactions occurring inside the cell can be described as follows [7]:

$$\text{Positive electrode:} \quad \mathrm{LiMO_2} \rightleftharpoons \mathrm{Li_{1-x}MO_2} + \mathrm{xLi^+} + \mathrm{xe^-} \tag{2.1}$$

$$\text{Negative electrode:} \quad \mathrm{C_6} + \mathrm{xLi^+} + \mathrm{xe^-} \rightleftharpoons \mathrm{Li_xC_6} \tag{2.2}$$

$$\text{Total cell reaction:} \quad \mathrm{LiMO_2} + \mathrm{C_6} \rightleftharpoons \mathrm{Li_{1-x}MO_2} + \mathrm{Li_xC_6} \tag{2.3}$$

Insertion of species into layered host structures without change in the chemical structure of the host material is called an intercalation reaction and the

resulting structures are generally called intercalation compounds. Such reactions occur in highly anisotropic layered structures where the intraplanar binding forces (forces acting between the atoms in a plane) are large in comparison with the interplanar binding forces (forces acting between the planes) of the host material [8].

Before looking into depth of the major components of secondary Li-ion batteries, some important parameters/properties of batteries will be outlined.

2.2.1 Critical parameters

Open-circuit voltage

In lithium-ion cells, the open-circuit voltage, V_{OC}, is given by the difference in electrochemical potential of Li between the cathode (μ_C) and the anode (μ_A) as the open-circuit voltage is given by the following equation:

$$V_{OC} = \frac{\mu_C - \mu_A}{F} \tag{2.4}$$

where F is the Faradays constant ($F = 96485$ C mol^{-1}).

The electrochemical stability of the cell is determined by the stability window of the electrolyte. The stability window lies in the energy range between the lowest unoccupied molecular orbital (LUMO) and the highest occupied molecular orbital (HOMO) of the electrolyte. This implies that the redox energies of the electrodes are required to lie within the band gap E_g of the electrolyte. Potentials on the anodes above LUMO will reduce the electrolyte, and potentials on the cathode below HOMO will oxidize the electrolyte unless a solid electrolyte interface (SEI) layer is formed to prevent such reactions [9]. Hence, the limitation on the cell voltage due to the requirement of electrochemical stability can be expressed as follow:

$$V_{OC} = \frac{\mu_C - \mu_A}{F} \leq E_g \tag{2.5}$$

The SEI layer is further described in section 2.5.1.

Capacity

The theoretical capacity of a battery is a measure of its ability to store electrical charge. The theoretical capacity of a battery cell is determined by

the amount of active materials in the cell and it is expressed as the total quantity of electricity involved in the electrochemical reaction and defined in terms of coulombs (C) or ampere-hours (Ah) [6]. In order to achieve high capacity, the electrode materials should be able to convert or intercalate high number of charge carriers.

Cycle life

In Appendix A of *Handbook of batteries* [6] the cycle life is defined as "The number of cycles under specified conditions which are available from a secondary battery before it fails to meet specified criteria as to performance". The capacity of a battery decreases with the number of cycles performed. When the capacity has decreased to 80 % - 60 % of its original capacity (before cycling), the battery is no longer considered to be usable [10].

Charge/discharge rate

When describing batteries, discharge and charge currents are often expressed in terms of C-rates. The C-rate is a way to express the rate at which the battery is discharged relative to its maximum capacity, which differ for the different battery compositions. A discharge current of 1C means that the entire battery will be discharged in 1 hour. In other words, for a battery with a capacity of 100 Ah this corresponds to a discharge current of 100 A. For the same battery a 5 C rate would be 500 A and a C/2 rate would be 50 A [11].

Rate capability

The rate capability of a battery is a measure of its ability to deliver current. In the work of Ramadass *et al.* [12], where the capacity fade of Sony 18650 cells was investigated, the rate capability of a Li-ion battery was defined as the maximum continuous or pulsed output current the battery can provide. The rate capability is important when deciding the cycle life of a Li-ion battery cell. Battery cells with higher rate capability have, in general, higher power densities and better cycle life compared to cells with poor rate capability. Additionally, batteries with high rate capability tolerate higher charging currents than batteries with lower rate capabilities [10] .

2.3 The positive electrode

The first generation of Li-ion batteries were based on lithiated cobalt (Co) oxide cathodes, which by 2010 accounted for more than half of the cathode chemistry in cells manufactured worldwide [13]. The worldwide interest for $LiCoO_2$ as cathode material in these batteries is due to its performance of high specific capacity, low self-charge and excellent cycle life [14]. But despite the fact that $LiCoO_2$ is a successful cathode material, alternative materials are being developed in order to decrease the cost and improve stability [15]. Other commonly used materials for the positive electrode are $Li(Ni,Mn,Co)O_2$, $LiMn_2O_4$ and $LiFePO_4$. Some of the key requirements for a successful cathode material are listed in [9]:

- The intercalation cathode $Li_xM_yX_z$ (X = anion) should have a low chemical potential (vs. Li/Li^+) in order to maximize the cell voltage.
- In order to maximize the cell capacity, the intercalation compound should allow for large number of lithium ions per formula unit.
- For good cycle life, intercalation/extraction reactions should be reversible, with minimal or no change in structure upon intercalation.
- The intercalation compound should possess both good electronic conductivity and good lithium-ion conductivity to ensure minimization of polarization losses during cycling and by that support fast charge-discharge rates and power density. The lithium-ion and electronic conductivities depend on the crystal structure, arrangement of the MX^n polyhedral geometry, interconnection of lithium sites, electronic configuration and relative positions of the Mn^+ and X^{n-} energies.
- As already mentioned in Section 2.2.1, the redox energy of both anode and cathode should lie within the band gap of the electrolyte.
- The material choice for the cathode should also be inexpensive, environmentally benign and thermally and chemically stable.

The material of choice in this work is the spinel oxide cathode $LiMn_2O_4$. Mn is inexpensive and environmentally benign compared to Co and Ni involved in the layered oxide structure, and the spinel $LiMn_2O_4$ has hence become an attractive cathode material [9]. Figure 2.2 shows the crystal structure of the spinel $LiMn_2O_4$.

According to the study done by Aydinol *et al.* [16] the extraction/insertion of two lithium ions from/into the $LiMn_2O_4$ spinel framework occurs

in two distinct steps. Around 4 V Lithium intercalation/de-intercalation into/from the 8a tetrahedral sites will occur with the maintenance of the initial cubic symmetry. intercalation/de-intercalation into/from the 16c octahedral sites occurs around 3 V by a two-phase mechanism involving the cubic spinel $LiMn_2O_4$ and the tetragonal lithiated spinel $Li_2Mn_2O_4$. The transition from cubic to tetragonal structure upon lithium insertion/extraction of 16c octahedral sites results in change of the unit cell volume by up to 6.5 %, and discharge- charge cycling in the 3 V region is a challenge in the use of $LiMn_2O_4$. Therefore, $LiMn_2O_4$ can only be used in the 4 V region where it has a limited practical capacity of approximately 120 mAh/g [9, 15]. Another origin of the capacity fading of $LiMn_2O_4$-based cathode materials is related to Mn^{2+} dissolution from the spinel into the electrolyte, especially at elevated temperatures [2, 17]. The latter is believed to be the main cause for capacity fades in these materials.

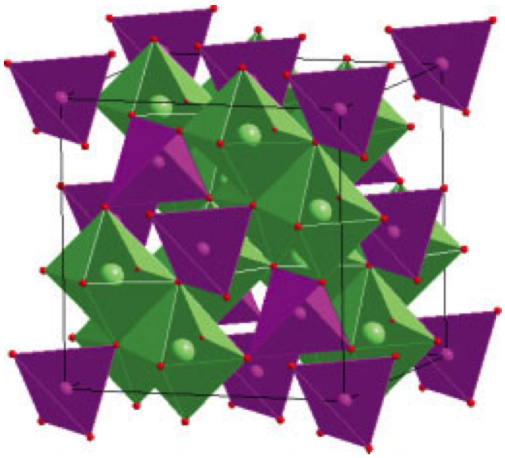

Figure 2.2: Crystal structure of the spinel structure, $LiMn_2O_4$ [9].

The fairly low electronic conductivities of the most common cathode materials (e.g. 10^{-6} S cm^{-1} for $LiMn_2O_4$ [2]) do not enable all of the active material to be utilized, and cause low battery cycle ability. A numerical study by Chen *et al.* [18] further concludes that neither surface nor bulk modifications of active-material particle conductivities seem desirable targets for improvement of conductivity in cathode materials. By contrast, the same study arrived at the conclusion that conductive coating and addition of conductive additive to such materials could improve the conductivity by values 25 times larger than the bulk conductivity of the active material. Li-ion battery cathodes are typically composite cathodes consisting of particles of active material, polymeric binder and conductive additive. Figure

2.3 illustrates how the components of the cathode are mixed. The different components and the cooperation between them play an important role in determining the physical and electrochemical properties of the electrode. The active material is the host for intercalated lithium stored in the electrode. The binder is responsible for binding the active materials and conductive additive together and assures adhesion to the aluminum current collector. The last component, the conductive additive, is required to ensure conductivity in the binder phase [19].

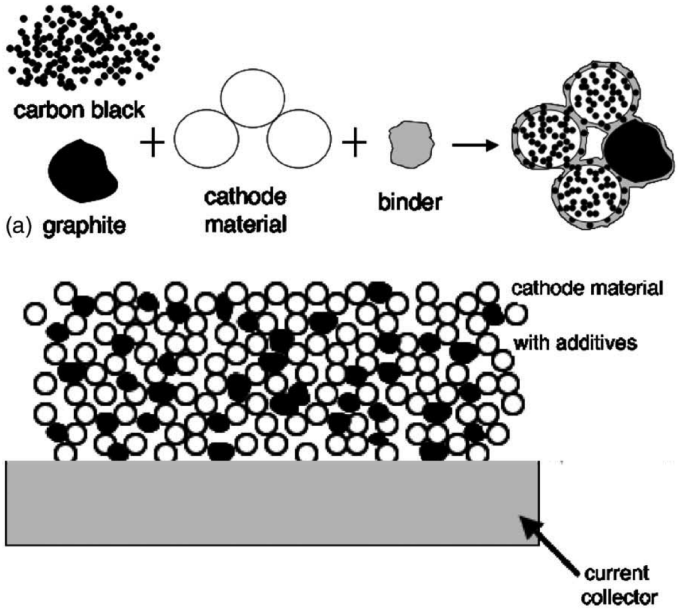

Figure 2.3: An illustration of how the different components are mixed for the positive electrode. Modified from [18].

As described by Hong *et al.* [20] it is generally accepted that the role of the conductive additive is to enhance the electrode conductivity by filling the free spaces made by the grains of active material to form a continuous network. Another important role of the conductive additive is to absorb and retain electrolyte solution. This allows intimate contact between the Li-ions and the active material, which enables better utilization of the active material. On the other hand, the two inactive electrode components are confined by the other, due to the competition between the ion blocking effect of the binder and the electronic effect of the conductive additive [19]. As the conductive additive is only improving the electronic conductivity and not involved in the reaction which delivers the energy of the cell, the amount of the conductive additive has to be minimized.

Upon electrode preparation, a homogeneous dispersion of the active material and conductive additive throughout the electrode is important because the cell polarization and utilization of active material is determined by this feature. Several parameters affect the dispersion of the electrode, such as particle size and shape, density, volume fraction of individual components, and inter-particle interaction forces. Thus, selection of materials, mixing and coating method should be deliberately selected [20].

2.4 The electrolyte

In this section, principles behind the electrolyte behavior and the requirements of electrolytes for use in Li-ion battery systems will be reviewed. The theory is mainly based on two review articles by Xu [13, 21].

Numerous electrolyte compositions for use in Li-ion batteries have been developed and the majority is based on solutions of one or more lithium salts in mixtures of two or more solvents. Sometimes additives are also added to the mixture. The reason for the mixed solvent formula is due to diverse and often contradicting requirements of battery applications, which hardly can be met by any compound alone, for example, high fluidity simultaneously with high dielectric constant. To achieve electrolytes that meet various requirements simultaneously, solvents of very different natures are often used together [21].

The main function of an electrolyte is to prevent direct electronic contact between the electrodes and thus assure an orderly and steady electron flow in the outer circuit. At the same time, the electrolyte must possess a high ionic conductivity in order to maintain the internal charge transfer [22]. Besides, the electrolyte should also fulfill several more essential requirements in order to make sure that the resulting battery function as desired. The perhaps most important property is the electrochemical stability of the electrolyte during operation. This entails that the electrolyte should be inert and stable against the possible reactions that may occur on the electrodes, which is oxidative decomposition on the positive electrode and reductive composition on the negative electrode. There are two ways to achieve this requirement:

(1) All electrolyte components are thermodynamically stable under operation conditions.

(2) The electrolyte components decompose into protective products on the electrode surface, forming an effective passivation that will prevent sus-

tained decomposition of electrolyte components.

As the voltage range of most Li-ion batteries exceeds beyond the stability window of the electrolyte, the requirement is obtained by passivation layer formation. Wide temperature range, high safety and low toxicity are other important requirements [13, 22].

As previously stated, the ionic conductivity of electrolytes is of major concern. The ability to conduct ions will determine how fast the energy stored in electrodes can be delivered. Maintenance of ionic conductivity is the primary reason for solvent mixing in the electrolyte. Equation 2.6 expresses ionic conductivity:

$$\sigma = \sum n_i \mu_i Z_i e \tag{2.6}$$

where n_i is the free ion number, μ_i is the ionic conductivity, Z_i is the valence order of ionic species i, and e is the unit charge of electrons. To display high values for all these parameters, the electrolyte must have contradicting properties.

As summarized in [21] the skeletal components of the electrolyte for the commercialized lithium-ion devices have been identified. The overwhelming majority of electrolyte compositions used in various brands of commercialized lithium-ion devices are based on two indispensable components: EC as the solvent and $LiPF_6$ as the salt. As listed in Table 1 in Xu´s review article [21], EC has a quite high melting temperature ($T_b = 36.4°C$) and a high dielectric constant ($\epsilon = 89.78$ at 25°C). High dielectric constant implies ability to coordinate large number of ions, which is often associated with high viscosity. By contrast, low viscosity improves ion mobility in the electrolyte. In order to increase the fluidity and reduce the melting point of the electrolyte, a linear carbonate, e.g. DMC, DEC, EMC, are used as co-solvents, forming the electrolyte composition $LiPF_6$/EC/linear carbonate(s).

Electrolyte additives

To improve Li-ion battery performance, use of electrolyte additives is one of the most economic and effective methods. Presence of electrolyte additive may significantly improve cycleability and cycle life of the battery, usually by addition of amounts no more than 5 vol% or 5 wt%. In the review article on electrolyte additives for lithium-ion batteries by Zhang [23], several features of different electrolyte additives for better battery performance are listed:

1. Facilitate formation of SEI on the anode (graphite) surface.
2. Reduce irreversible capacity and gas generation for the SEI formation and long-time cycling.
3. Enhance thermal stability of $LiPF_6$ against organic electrolyte solvents.
4. Protect cathode material from dissolution and overcharge.
5. Improve essential physical properties of electrolyte.

As this list indicates, there exist several types of electrolyte additives with different functions in improving Li-ion battery performance. In his review article, Zhang [23] describes several different types of additives in more detail. In the following the focus will mainly be on the electrolyte additives similar to the one used in this work.

As will be described later in Section 2.5.1, the main inorganic components in the SEI formed on the anode surface in cells with $LiPF_6$-carbonate electrolytes are known to be Li_2CO_3 and LiF. Isolated LiF crystals have been identified as the important factor causing instability of the SEI layer [23, 24]. Thus, several different boron-based anion receptors have been developed in order to dissolve LiF. The most represented is the tris(pentafluorophenyl) borane (TPFPB). It has been reported that addition of restricted amounts of TPFPB will improve the cycleability and capacity retention of Li-ion cells with $LiPF_6$ electrolytes. According to the study by Chen *et al.* [25] a content of TPFPB below 3 wt% was desirable to maximize the power capabilities of lithium-ion batteries. However, the optimal content of TPFPB is determined by the choice of electrolyte. They further conclude that TPFPB participates in the formation of passivation films and dissolution of the LiF in the films, as well as to improve the transport of lithium ions through the passivation films. On the other hand, high concentrations of TPFPB may result in increased impedance across these films, decreasing the power capabilities of lithium-ion batteries.

Sun *et al.* [26] also came up with the conclusion that Li-ion cells with TPFPB were able to deliver higher capacity than cells without TPFPB in prolonged cycling.

Another negative impact by use of TPFPB is that it may capture LiF from $LiPF_6$ and release PF_5, which is a highly reactive compound. PF_5 accelerates deterioration of the electrolyte solvents, as illustrated by Equation 2.7 [23, 25]:

$$LiPF_6 + BX_3 \rightleftharpoons LiBX_3F + PF_5 \tag{2.7}$$

Here, X represents tris(pentafluorophenyl) group.

From the results seen in literature, it is clear that the amount of TPFPB added to the electrolytes is very crucial in order to achieve the favored reactions. As the electrolyte additive used in this work (tris(hexafluoroisopropyl)borate (THFIPB)) is also a boron-based anion receptor, similar trends are expected.

Another study by Li *et al.* [27] regarding Li-ion batteries using LiF salt and the boron-based anion receptors previously presented show that the transfer numbers of Li-ions are also higher in electrolytes containing anion receptor and LiF salt, indicating effective lithium-ion conductivity.

2.5 The negative electrode

The most common intercalation compounds for the negative electrode are derived from graphite as many chemical species (anions, cations and/or molecules) can be intercalated into graphite and form graphite intercalation compounds (GICs). The graphite structure consists of carbon atoms arranged in hexagonal rings (a honeycomb network, [28]), stacked in an orderly fashion. Between these graphene layers only weak van der Waals bonds exists. Figure 2.4 shows the most usual structure of graphite, the hexagonal graphite, with stacking sequence ABABAB.. . A structure found less frequently is the graphite with stacking sequence ABCABC.. and that is called rhombohedral graphite. The interplanar layer distance (d_{002}) in graphite is 0.3354 nm as shown in Figure 2.4, while the C-C bond distance in the direction parallel to the layer planes is 0.142 nm.

From the figure it is apparent that graphite has two distinct surfaces present, basal planes and edge planes [29]. Intercalation of lithium-ions into graphite proceeds via the edge planes in the carbon host structure. Intercalation through basal planes can only take place at defect sites [7, 30]. This is due to the highly anisotropy physical properties of graphite. For instance, the difference in electrical conductivity between the direction parallel to the basal plane and the direction perpendicular to the basal plane is in the order of factor 100 [29].

A characteristic feature of these compounds (GICs) is the staging phenomenon, which is characterized by periodic arrangement of the intercalated layers

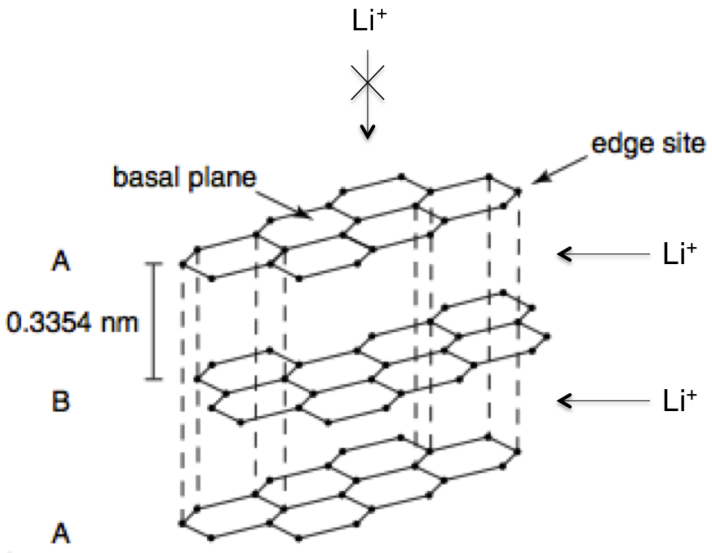

Figure 2.4: A schematic illustration of hexagonal graphite. The insertion mechanism of Li^+ into graphite is displayed. Modified from [29].

within the graphite structure [7, 30]. This staging phenomenon can be seen in voltage-capacity curves and is illustrated in Figure 2.5.

The various GICs are classified according to the number of graphene layers separating the two nearest intercalated layers by the stage index n. The intercalation of lithium into graphite proceeds through formation of the following compounds [7]:

- stage-4 (composition not well defined)
- stage-3 (LiC_{24})
- a dilute lattice gas disordered stage-2 (LiC_{18})
- stage-2 (LiC_{12})
- stage-1 (LiC_6)

The potential plateaus in the voltage-capacity curve represent two-phase regions where phase transitions between successive stage-n phases during the Li-ion intercalation/de-intercalation occur. The reversible intercalation/de-intercalation of lithium-ions occurs at potentials below $\sim$ 0.20V vs. Li/Li^+ and the transitions between the given compounds occurs at 0.20V, 0.14V, 0.14V, 0.12V and 0.09V vs. Li/Li^+ during intercalation, respectively [7].

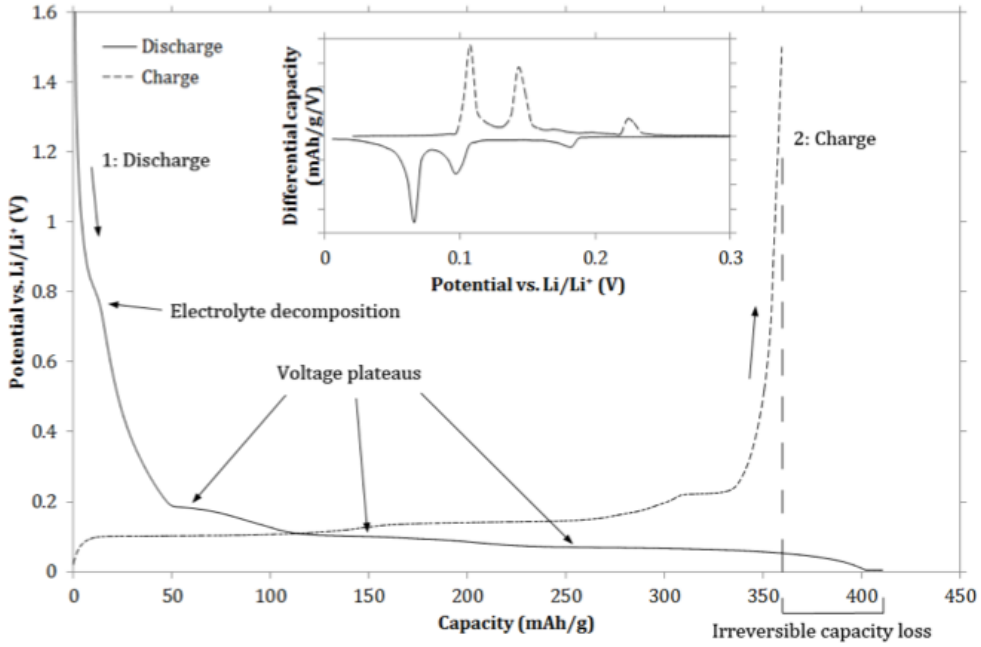

Figure 2.5: Voltage-capacity curve of the initial discharge-charge cycle of a Li/graphite half-cell. The different intercalation stages in the initial cycle are indicated, along with the irreversible capacity loss (ICL). The insert shows the differential capacity vs. voltage, displaying the three main intercalation stages upon discharging and charging [22].

2.5.1 Solid electrolyte interphase (SEI) formation

As lithium is among the most electronegative of the elements (-3.04 V vs. standard hydrogen electrode [31]), there are almost no solvents or salts that can remain thermodynamically stable in electrical contact with lithium. The explanation for the apparent stability of lithium metal in non-aqueous electrolytes is that electrolyte components are reduced upon contact with lithium, depositing decomposition products on the lithium surface and thereby forming a film which is electrically insulating, but at the same time permeable to ions [13]. This protective electrolyte film was named solid electrolyte interphase (SEI) [32].

As earlier introduced, graphitic carbons serve as anode material in commercial lithium-ion batteries. By use of carbon anodes instead of metallic lithium, formation of lithium dendrites on the anode surface are avoided upon charging and reliability and safety of batteries are obtained [33]. Since

the intercalation potential is in close proximity ($\sim$ 0.20 V vs. Li) to that of lithium metal, a solid electrode interphase was assumed by Aurbach *et al.* to also be present at the interface between the graphitic anode and the electrolyte in order to stop electrolyte decomposition [13, 34]. Due to its low redox potential close to Li^+/Li, good cycling stability, low cost and environmental friendliness, graphite is today exclusively utilized as the negative electrode material for commercial lithium-ion batteries [35].

At present, there is an agreement that a solid electrolyte interphase layer will be formed on the surface of the graphite anode during the first charge of a Li-ion cell [35]. As previously outlined in Section 2.4, the performance of batteries is greatly influenced by the choice of electrolyte due to differences in conductivity and wettability. But properties of the formed SEI layer on the electrode surfaces are also of major importance for the battery performance and this will be the focus for this section [36].

Influence of the electrolyte composition on the SEI

The formation and resulting composition of the SEI layer is dependent of several factors, electrolyte composition being a key factor. Several SEI components are known to appear only in electrolytes containing specific solvents, but still there is no general agreement regarding the specific SEI composition and the explicit influence of the electrolyte. Various compositions have been proposed, yet there are some general features and major components for specific electrolyte compositions that have been identified [22, 37]. The SEI layer consists of both inorganic and organic species. Figure 2.6 illustrates a general SEI composition, consisting of a dense inorganic layer close to the surface and on top of this a porous organic layer [35, 36, 38].

The cyclic structured organic carbonates EC and PC, and the acyclic structures, like dimethyl carbonate (DMC), diethyl carbonate (DEC), ethyl methyl carbonate (EMC) are the main solvents used in commercial Li-ion batteries. The reason for mixing linear and cyclic carbonates is, as indicated earlier, to compromise between the solubility of the salt and conductivity of the solvent [36] .

PC-based electrolytes were originally the choice for lithium-ion batteries. The problem within these cells was that the graphite electrode underwent a rapid change in ability of lithium intercalation. This was generally caused by co-intercalation of PC molecules into the graphite structure before formation of reductive decompositions with Li-ions [35]. As explained by Xu in is review

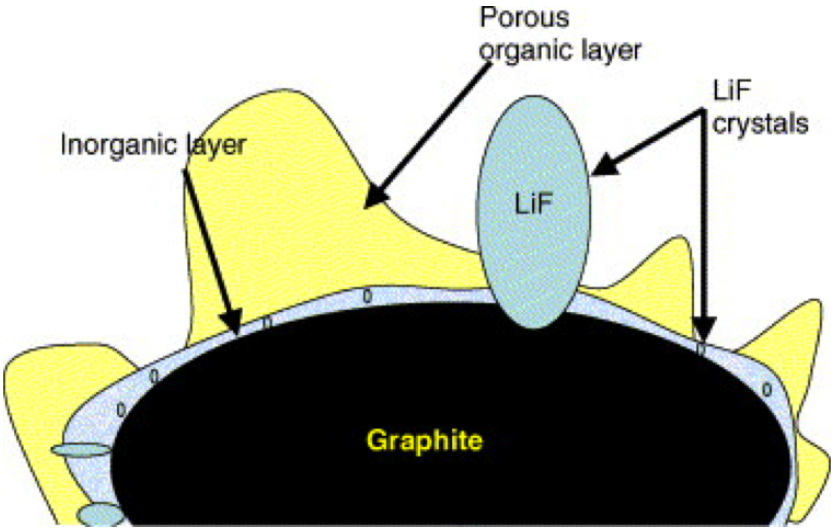

Figure 2.6: A schematic illustration of the SEI layer on a graphite particle [39].

article [13], the decomposition product of PC through single-electron pathway happens to be unable to protect the layered structure of graphite from exfoliating at $\sim$ 0.70 V vs. Li, and consequently lithium intercalation will not occur reversibly. By replacement of PC by EC, an interphase enabling reversible lithium intercalation chemistry at potentials close to that of Li metal electrode was created, thus laying the foundation for Li-ion technology [13].

Two reaction mechanisms have been proposed for the reduction of carbonate-based solvents, e.g. EC, as shown in Figure 2.7 [40]. Both mechanisms are present in the process of SEI formation and are competing mechanisms. According to the review Zhang [40], the two mechanisms result in SEI with different properties. If mechanism (I) is predominant, more gaseous products are formed upon solvent reduction and the resulting SEI is Li_2CO_3-abundant and less stable. On the other hand, if mechanism (II) predominates, less gaseous products are formed and the resulting products are substantially insoluble in the electrolyte leading to a more compact and stable SEI.

Another study by Aurbach *et al.* [41] showed that when EC or PC concentrations in the electrolyte are high, then $(CH_2OCO_2Li)_2$ or $ROCO_2Li$ are the major reduction products, respectively. On the other hand, when EC and PC concentrations are low, Li_2CO_3 is the major reduction product. CH_2OCO_2Li and Li_2CO_3 are generally better passivation compounds than ROLi and $ROCO_2Li$ due to their lower solubility in the solvents. Accor-

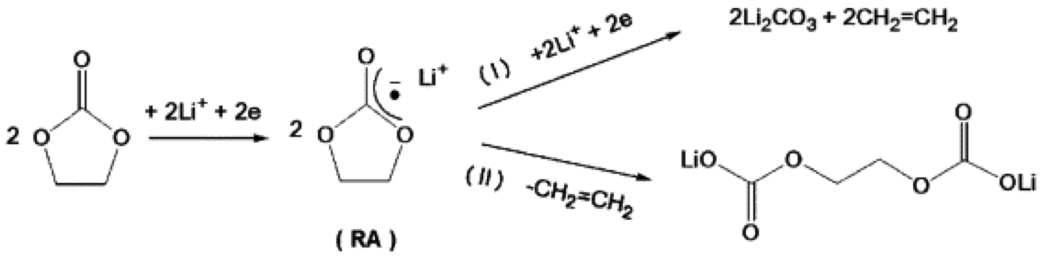

Figure 2.7: Illustration of the two mechanisms proposed for the electrochemically induced reduction of carbonate-based solvents, i.e. ethylene carbonate (EC). RA in the figure is a radical anion [40].

ing to Verma *et al.* [37] this is in agreement with another study were EC reduction products were shown to be insoluble and thus more passivating. This highlights the importance, not only of the choice of components for the electrolyte, but also the composition ratio of the different components.

Another well established aspect of SEI formation is that the type of lithium salt in the electrolyte influences the ratio of inorganic and organic components in SEI layer. LiF formed close to the electrode surface is mainly a salt reduction product ($LIPF_6$, $LiBF_4$ and $LiAsF_6$) [39], but can also be formed because of electrolyte impurities interacting with the initially formed film [36]. Temperature, trace impurities and organic solvent reactions are factors influencing the amount of LiF that is formed in this layer [39].

Unfortunately, there is a contradictory relationship between lithium conductivity and SEI stability. Highly conductive SEI layers are in general less passivating than a compact passivation layer with lower conductivity and high resistance. Presence of Li_2CO_3 is beneficial for film passivation, but is causing an increase in interfacial resistance. LiF are also increasing the interfacial resistance between the electrolyte and electrode surface [36].

Influence of the graphite electrode on SEI

As SEI is an interphase between the electrolyte and the active material, it is to be expected that the active material also influences on the properties of the SEI.

Many researchers indicates that morphology and chemistry of the graphite surface affects the two mechanisms, shown in Figure 2.7, and that they are associated with the catalytic activity of the fresh graphite structure [40]. The strong location-dependence of SEI composition observed by Peled *et al.* [42]

confirms this catalytic effect. This is shown in Figure 2.8, where the SEI layer on edge areas of the graphite is mainly dominated by inorganic compound, whereas the SEI on the basal plane areas is enriched with organic compounds [37, 40, 42].

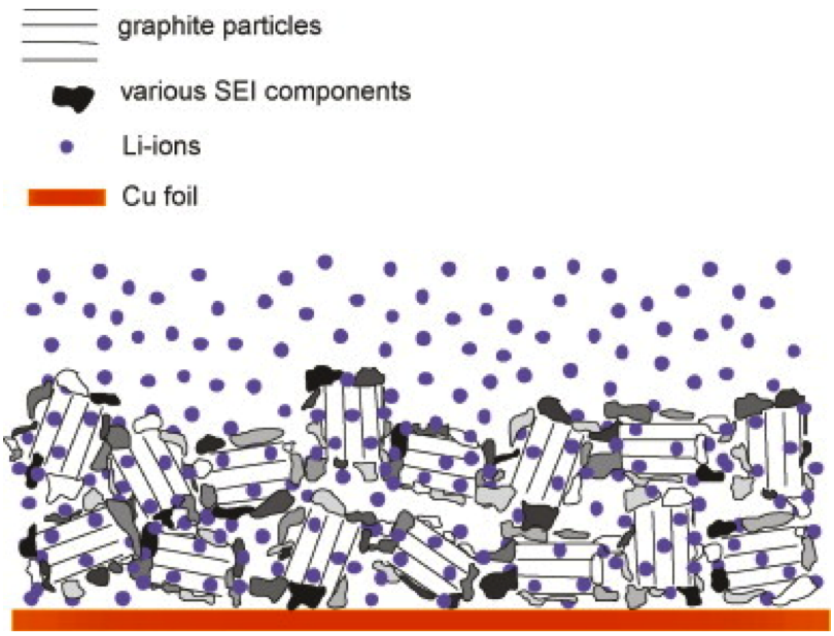

Figure 2.8: Sketch of a lithiated graphite composite electrode covered by an inhomogeneous SEI layer. The darker shades of gray are mainly inorganic components in the SEI, whereas the ones shown in lighter shades are organic [37].

To summarize, as done by Verma *et al.* [37], the features of an ideal SEI are as follow:

- The SEI should have minimum electronic and maximum Li-ion conductivity.
- Formation kinetics should be fast, allowing complete SEI formation before onset of Li-ion intercalation.
- Morphology and composition should be uniform.
- The SEI should contain stable and passivating compounds rather than metastable and poorly passivating ones (Li_2CO_3 rather than ROLi and $ROCO_2Li$).
- The SEI should adhere well to the carbon structure.

- The SEI should be elastic and flexible to withstand non-uniform electrochemical reactions.

2.6 Cell impedances

Minimization of the overall resistance in electrochemical cells is the key to obtain batteries with high-power capability [43]. All key phenomena in Li-ion cells for secondary batteries involve conducting charged particles (electrons and ions) back and forth between the electrodes. The operating voltage (E) of battery cells is, in general, lower than the standard cell potential (E_0) due to several factors causing potential drops [5]. This is stated mathematically by Equation 2.8 [6]:

$$E = E_0 - [(\eta_{ct})_a + (\eta_{ct})_c] - [(\eta_c)_a + (\eta_c)_c] - iR_i = iR \tag{2.8}$$

where E_0 is the standard cell potential, $(\eta_{ct})_a$ and $(\eta_{ct})_c$ are activation polarizations (charge transfer overvoltage) at the anode and cathode, $(\eta_c)_a$ and $(\eta_c)_c$ are concentration polarizations at the anode and cathode, i is the operating current, R_i is the internal resistance of the cell and R is the total resistance.

Activation polarizations are given by the kinetics of charge transfer whilst concentration polarizations are given by the rate of mass transfer. Conduction properties of various materials and their interfaces are affecting the internal resistance, which can be divided into ionic resistances, electronic resistances and interfacial resistances [5].

Figure 2.9 illustrates the journey of a Li-ion from the solution bulk to the graphite interior with he associated impedances. Studies by Abe *et al.* [44] have identified the de-solvation process at the graphite electrode/electrolyte interphase to be very important in lithium-ion transfer kinetics. In the review by Xu [13] it is stated that this step is largely responsible for the cell impedance in Li-ion cells at low temperature or under high drain rate applications.

A more recent study by Wu *et al.* [45] comments on of the rapid advancement in material synthesis technologies and points out that the ionic and electronic resistances of active materials to some extent have become competitive to the other resistance sources in the cell.

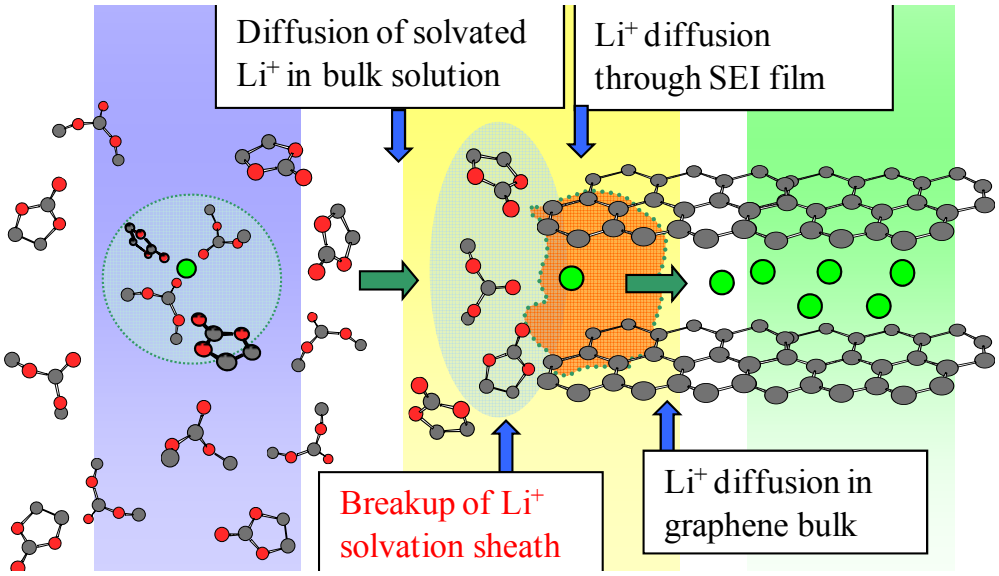

Figure 2.9: A solvated Li-ions journey from the solution bulk to the graphite interior, illustrating the associated impedance components. Modified from [13].

2.6.1 Coating of current collectors

As the ionic and electronic resistances of Li-ion batteries has been lowered due to rapid advancement in material synthesis technologies, the resistance of the interface between the current collector and the active layer in batteries has received increased attention.

Investigations of charge/discharge capacity and cycle stability at high C-rate of $LiFePO_4$ electrodes were performed by Wu *et al.* [43], using three types of Al current collectors. The aluminum current collectors used were a smooth un-etched Al-foil, an anodization-etched Al-foil and the etched Al-foil covered with a conformal C coating grown at 600°C in CH_4. The carbon coated current collector showed increase in power-delivering capability as well as great enhancement in cycle stability at high C-rate.

In their later study on the effect of current collectors on power performance of $Li_4Ti_5O_{12}$ anode for Li-ion battery [45] they also found that a C coating produced by a chemical vapor deposition process on Al and Cu current collectors markedly enhanced the power performance of these electrodes. Investigation and comparison of an Al-foil and an anodized-etched carbon coated Al-foil for use as current collector showed an increase in capacity of 20 % under 1 C and 150 % under 20 C. In the same study they found that cells with

Cu as current collector exhibited higher capacities than cells with Al and anodized-etched Al. Discharge voltage curves at 3 C rate depicting their results are shown in Figure 2.10. The active layer of their cells consisted of, on a dry basis, 80 wt.% LTO powder (BTR Energy Materials Co., Ltd; average particle size (vendor's value: ca. 100 nm), 13 wt.% carbon black, and 7 wt.% binder (polyvinylidene difluoride; Aldrich) [45].

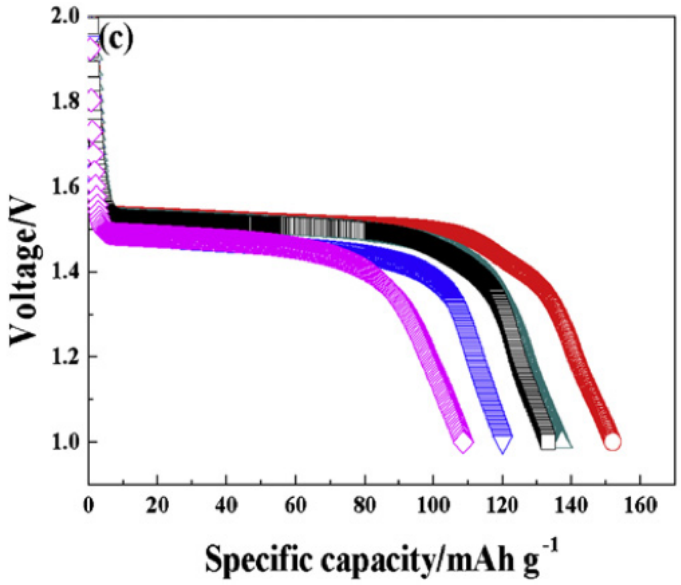

Figure 2.10: Discharge voltage curves (3C rate). (◯: Cu-foil with a C coating, □: Cu-foil, △: Anodization-etched Al with C coating, ▽: Anodization-etched Al, ◊: Al). Modified from [45].

They ascribe the resistance reduction of the current collector/active material interface to change in surface characteristics. Oxide layers present on the surface of pristine Al and Cu, result in significant electrical resistance between active materials and current collectors. In addition, the oxide surface is hydrophilic, unlike the coating slurry and dried active material, which are both hydrophobic by nature. Different polarities of current collector and active material would result in poor adhesion, and hence high interfacial resistance. According to the two studies by Wu *et al.* [43, 45] the C coating can significantly reduce these problems by (1) directly reducing of surface resistance by destroying the oxide layer and (2) turn current collector surfaces from hydrophilic to hydrophobic.

2.6.2 Additional factors affecting the rate capability

Several factors influence the rate capability of lithium-ion batteries. For the electrodes, especially the cathode, good electronic network, high Li-ion diffusion rates in the solid and good transport properties of Li-ions in the electrolyte are crucial. For the anode, additionally important is that the resistance of the solid electrolyte interface (SEI layer) is as low as possible.

The following lithium metal oxides, $LiCoO_2$, $LiMn_2O_4$ and $LiFePO_4$, are some of the most commonly studied cathode materials for lithium ion batteries. They are considered as promising Li-ion cathodes materials because of their low price, relative safety, and environmental friendliness [46]. Unfortunelately, the electronic conductivity of these materials are fairly low and can often impair the rate capability. Electron conductive additives are commonly added to such materials to improve their electrochemical properties [2].

In this work, two different conductive additives have been investigated for use in cathode materials of Li-ion batteries. As demonstrated by Chen *et al.* [18] , the addition of conductive additives to cathode materials improve capacity, via reduction of internal resistance and cycleability.

Crystalline carbons usually display higher electronic conductivities than conventional carbon additives such as carbon black. Graphene has an extremely high surface/mass ratio, and its structure (one single layer of graphite) assures one of the highest electron conductivities. This makes graphene exceptionally well suited for use as conducting additive in lithium ion battery cathodes [2].

A study by Buqa *et al.* [47] demonstrated that TIMREX SFG synthetic graphite material of varying particle size distribution was capable of very high discharge rates of up to 20 C for thin graphite electrodes with a low electrode loading (1.5 mg/cm^2). They further concluded that in more practical designs for lithium-ion batteries, a 70-80 μm electrode could still reach a discharge rate capability of 10 C. However, their most important concluding remark is that electrode engineering, not the graphite material itself, is the limiting factor of electrode rate capability. Hence, the loading, thickness, and porosity of the electrodes are key parameters with major impact on the rate capability.

The same article [47] claims that lithium accumulation on the graphite surface is believed to be higher for larger particles than for smaller particles. Hence, the thickness of SEI is usually thicker on the surface of larger particles. In graphite electrodes with smaller particles there is better contact

between the particles resulting in a more uniform potential distribution end hence, a more compact SEI. Thus, they conclude that in addition to the electrode engineering, there is an indirect influence of the SEI on the rate capability of graphite electrodes.

2.7 Characterization methods

2.7.1 Raman spectroscopy

The Raman effect was discovered in 1928 by the Indian physicist C. V. Raman together with K. S. Krishnan [48]. The Raman effect is the inelastic scattering of incident photons on a molecule due to interactions with the vibrational modes of the molecule. Inelastic scattering means change of the frequency of the incoming photons due to interaction with the sample. The vibrational modes are characteristic for each molecule and the energy of the scattered photon is dependent on the molecule in which the incident photon has interacted with. The Raman spectroscopy is one of the most powerful tools for study of carbonaceous materials as it possesses the ability to provide unique structural information from all types of compounds due to the uniqueness of the vibrational modes of a molecule [10]. Advantage of this spectroscopy technique is that it is quick, non-destructive and it requires little sample preparation.

Raman spectroscopy of graphite

Graphite has two Raman active vibrational modes, referred to as E_{2g1} and E_{2g2}, as illustrated in Figure 2.11. The E_{2g2} mode has been observed as a peak in perfectly crystalline carbon materials at around 1582 cm^{-1}, which is inherent in all carbon materials. At around 3248 cm^{-1} the same mode appears as a peak and is referred to as an overtone of the E_{2g2} mode. The second mode, E_{2g1}, is less known and has been theoretically estimated to appear at 210 cm^{-1} as a peak [10].

The Raman shift for carbonaceous materials is divided into first and second order regions after Tuinstra and Koenig (1970) [50, 51]. The first order region appears between 1100 and 1800 cm^{-1} and is the one considered in this work. This region consists of a characteristic peak for carbon materials in the range 1575 -1582cm^{-1} [28, 49, 51, 52]. This peak is referred to as the G peak and is due to the active mode E_{2g2}. Figure 2.12(a) shows the Raman spectrum

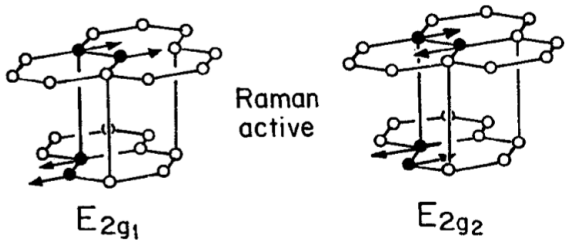

Figure 2.11: The Raman active vibrational modes of graphite. Modified from [49].

of a perfect crystalline material, where the G peak will be the only peak visible. In graphite materials less perfect, a second peak will appear in this first region at around 1355 cm^{-1}. This peak is referred to as the D peak and according to Zòlyomi *et al.* [52] this is a disorder-induced band in which the intensity increases with increasing level of disorder. The Raman specter of commercial graphite is shown in Figure 2.12(b). Other peaks may also appear in this first region [50], but this will not be focused on in this work.

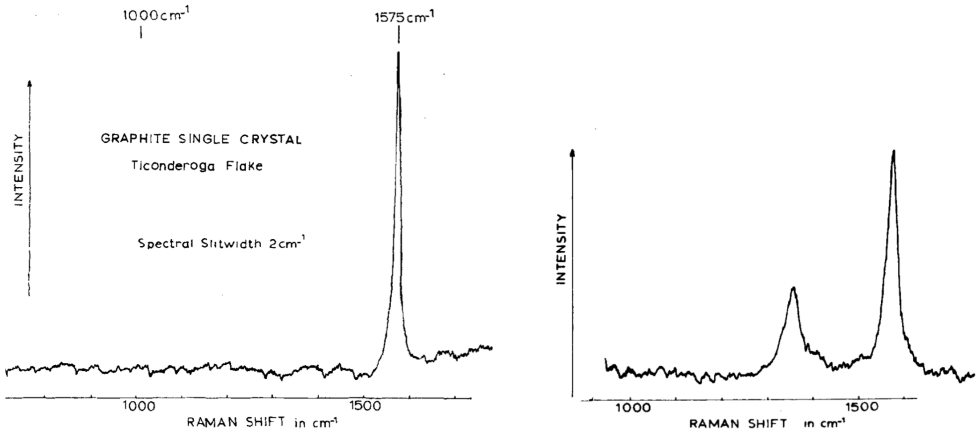

(a) (b)

Figure 2.12: Raman spectra of a single crystal of graphite (a) and a commercial graphite (b). Modified from [51].

Raman spectroscopy has also been used for characterization of graphene. The Raman spectra of graphene include the same peaks as graphite. As for graphite, the D-peak located at ∼1350 cm^{-1} will be absent in defect-free graphene. Zhu *et al.* claim that Raman spectroscopy could be used to distinguish the 'quality' of graphene and determine the number of layers (up

to five layers) by the shape, width and position of the D-peak. The D-peak will shift to higher wavenumber values and become broader as the number of layers increases [53].

The relative intensities of the D-peak (I_D) and the G-peak (I_G) can be used to calculate the crystallite size in the basal direction in the graphite structure, L_a. Tuinstra and Koenig (1970) [51] illustrates a linear relation between the R-ratio (I_D/I_G) and the ${L_a}^{-1}$ value. However, a modification of the equation used in their work has to be done when a HeNe laser of 632.8 nm is used, since an excitation wavelength of 488nm was used in that work. Goers *et al.* [28] present the equation that provides the relation between L_a and the R-ratio (I_D/I_G) and this is given in Equation 2.9.

$$L_a = \frac{4.4 \cdot f_L}{R} \quad R = I_D/I_G \tag{2.9}$$

where the correction factor f_L = R(632.8 nm)/R(488 nm) and gives approximately 2.2.

As elaborated by Tran [10], several different factors may affect the obtained R-ratio. Since Raman measurements are not the main focus of this thesis, the results extracted from Raman spectroscopy will be used for relative comparison of the samples investigated rather than concluding on exact values.

2.7.2 Scanning electron microscopy (SEM)

A scanning electron microscope (SEM) is a valuable characterization instrument for investigation of sample morphology, chemical composition, crystallite structure and orientation of the material making up a sample. A SEM uses a focused electron beam to generate signals at the surface of solids specimens. The signals are produced due to electron-sample interactions when the incoming electrons are decelerated in the solid sample [54]. These signals include secondary electrons (SE) (produce SEM images), backscattered electrons (BSE), diffracted backscattered electrons (EBSD) (used to determine crystal structures and orientations of minerals), photons (characteristic X-rays used for elemental analysis and continuum X-rays), visible light (cathodoluminescence - CL) and heat.

Figure 2.13 illustrates the relative penetration depths of the different signals. As this figure shows, the secondary electrons give signals from just underneath the surface and are therefore the signals most valuable for showing

morphology and topography of the samples.

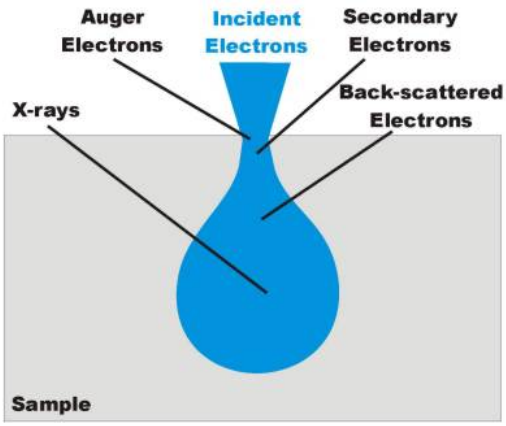

Figure 2.13: Signals in scanning electron microscopy. Modified from [55].

3. Experimental procedures

In this work, both anodes and cathodes were fabricated by tape casting onto current collectors, and tested electrochemically by galvanostatic cycling.

In addition to the electrode fabrication and electrochemical testing, coating of copper foils was conducted by use of the thermal CVD instrument at NTNU NanoLab. Preparations of two different electrolytes were conducted and Raman spectroscopy measurements were performed on coated and uncoated copper foils in addition to the two carbon conductive additives, in order to investigate the structure of the carbon coating and the powders. SEM images were taken of the electrode materials and the conductive additives as well as finished electrode casts.

In the following sections the experimental procedures will be described in more detail.

3.1 Materials

For the negative electrodes, a synthetic graphite (CPreme®G8, ConocoPhillips) was used as active material with carbon black (Super P Li, Timcal) as conductive additive. For the positive electrodes, Lithium manganese(III, IV)oxide ($LiMn_2O_4$, Sigma-Aldrich) was used as active material. In addition to the carbon black used in the negative electrode, a graphene nanopowder (AO-2, Graphene supermarket) was investigated for use as conductive additive in the positive electrode. The electrolytes are described in detail in Section 3.3. Table 3.1 presents technical data for the chemicals/materials used in electrode manufacturing.

Table 3.1: Technical data on materials used in the electrode manufacturing.

Material	Name	Purity [%]	Manufacturer
CPreme®graphite	G8	-	CPreme
Lithium manganese oxide	$LiMn_2O_4$	> 99	Sigma-Aldrich
Carbon black	Super P Li	-	Timcal
Graphene nanopowder	AO-2	99.9	Graphene supermarket
PVDF binder	Kynar 761	100	Arkema
Copper foil	BF-PlainStainproof	> 99.8	Circuit Foil
Alumininum foil		99.45	Alfa Aesar
NMP	1-methyl-2-pyrrolidinone	99.5	Sigma-Aldrich

3.2 Electrode fabrication

This section describes in detail how the slurry preparations for the electrode casting were conducted.

3.2.1 The negative electrode

Slurry preparations for the negative electrode were started by mixing the binder, polyvinylidene fluoride (PVDF, Arkema), and the solvent, 1-methyl-2-pyrrolidinone (NMP, Sigma-Aldrich). The mixture was left for stirring for approximately two hours until the binder was dissolved. The beaker containing the mixture was covered with parafilm to reduce evaporation of the solvent. After dissolving the binder, carbon conductive additive was added to the mixture and the mixture was left covered for stirring for another hour.

The carbon material used as the active material was then added to an Al_2O_3-jar with five 30 mm Al_2O_3 balls together with the mixture containing PVDF, NMP and conductive additive. The jar was then placed in a planetary mill (PM100, Retsch) for two hours at a rotation speed of 150 rpm to ensure a homogenous mixture/slurry. The slurry was then transferred to an Erlenmeyer flask and left for stirring under vacuum for approximately one hour for removal of any possible air bubbles. Table 3.2 contains the recipe for the preparation of the negative electrode.

The resulting slurry was then casted onto a copper foil (Circuitfoil, ≥ 10 μm thickness), pre washed with ethanol, using the doctor-blade technique. A tape caster (K control coater, model K101) was used and the height of the doctor blade was set to approximately 150 μm, to obtain the final thickness

Table 3.2: Recipe for the CPreme® G8 electrode.

Material	Weight [g]
Graphite	10
Carbon black	0.9756
PVDF	1.2195
NMP	18.2927

desired for these experiments. The copper foil with the wet slurry film was then heated on top of the tape caster bed at 60 °C for approximately 30 min inside the fume hood in order to evaporate most of the NMP.

The cast was further transferred into a vacuum furnace (Binder Vacuum Drying Furnace VD23) and left for heating at 120 °C and vacuum (∼0 mbar abs) for 12 hours. The final heating step was done in the big antechamber of a glove box (MBRAUN LABMASTER SP). The cast was left inside the antechamber for another overnight heating process at 120 °C and vacuum. Thereafter, the electrode sheets were introduced into the glove box and stored under argon atmosphere where water and oxygen contents are below 1 ppm.

3.2.2 The positive electrode

Slurry preparations for the positive electrode were started out by adding the oxide material, PVDF, the conductive additive and NMP, in the given order, into a small sample holder for ball milling. This was then placed in a mill (MM2200, Retsch) with amplitude 70 for 20 min to ensure homogeneity in the resulting slurry. Table 3.3 and 3.4 list the recipes for the positive electrodes investigated in this thesis.

Table 3.3: Recipe for the $LiMn_2O_4$ + carbon black electrode.

Material	Weight [g]
$LiMn_2O_4$	1
Carbon black	0.0976
PVDF	0.122
NMP	3.04

The doctor-blade technique was used for casting of the positive electrode as well, and the height of the doctor blade was adjusted to approximately 220 μm, due to use of a thicker current collector for the cathode. The current collector used for the positive electrode was an aluminum foil (Alfa Aesar, $\geq$

Table 3.4: Recipe for the $LiMn_2O_4$ + graphene nanopowder electrode

Material	Weight [g]
$LiMn_2O_4$	1
Graphene nanopowder	0.0976
PVDF	0.122
NMP	2.94

25 μm thickness). The slurry was casted on the rough side of the aluminum foil. The heating steps for the positive electrode was equal to those for the negative electrodes, except for the temperature in the vacuum furnace and the big antechamber, which was set to 100 °C instead of 120 °C . Thereafter, these electrode sheets were also introduced into the glove box and stored under argon atmosphere, where water and oxygen contents are below 1 ppm.

3.3 Electrolyte preparation

Two different electrolytes were prepared and used in this work. Electrolyte preparation was started out by melting ethylene carbonate (EC, anhydrous 99 %, Sigma-Aldrich) in a heating cabinet at 40 °C for 2-3 hours. On regular basis, EC is stored in a bottle inside the glove box. Before the heating process could start the bottle had to be taken out from the glove box and it was important to assure that the bottle was completely closed so that no air got inside. When sufficient amount of EC was melted the bottle was quickly introduced into the glove box and the melted EC was transferred to smaller containers.

The different electrolyte components were then weighted out in the glove box and added to a beaker in the following order:

- Dimethyl carbonate (DMC, anhydrous $\geq$ 99 %, Sigma-Aldrich)
- Lithium hexafluorophosphate ($LiPF_6$, battery grade$\geq$99.99 %, Sigma-Aldrich)
- Ethylene carbonate (EC, anhydrous 99 %, Sigma-Aldrich)

The solution was left for stirring for $\sim$ 4 hours until the salt was dissolved. The final electrolyte was then transferred to small beakers and stored inside the glove box. Table 3.5 contains the amounts of the solvents and the salts in the first electrolyte.

This will be referred to as E1 throughout this thesis. The second electrolyte

Table 3.5: Recipe for electrolyte E1.

Material/Chemical	Weight [g]
DMC	2.2449
EC	1.1889
$LiPF_6$	0.5070

was made by the same recipe as the first, only doubled, and in addition, 1 wt% tris(hexafluoroisopropyl) borate (THFIPB, $\geq$ 95.0 %, TCI) was added to the electrolyte. Table 3.6 contains the recipe for the second electrolyte, henceforth referred to as E2.

Table 3.6: Recipe for electrolyte E2.

Material	Weight [g]
E1	5.0
THFIPB	0.0505g

3.4 Cell assembly

In this work, coin cells of stainless steel (CR 2016: SUS316L, Hohsen Corp.) of size 20.25 mm in diameter and 1.6 mm height where assembled to produce Li/graphite and Li/$LiMn_2O_4$ half-cells. In order to understand these systems compared to commercial Li-ion cells, a brief explanation will be given.

Because of their low electrochemical potential vs. Li/Li^+, both graphite and the lithium metal oxide will act as negative electrode in cell assembly with Li-metal as the counter electrode. Both electrodes, which previously is referred to as the negative and the positive electrode in accordance with commercial Li-ion cells, will act as cathodes in the resulting cells made for this work. Hence, discharge of the Li/graphite half-cells will imply lithium intercalation into the graphite structure, whilst charge means de-intercalation of the graphite electrode. For the Li/$LiMn_2O_4$ half-cells, the reactions upon charge and discharge will be the same as in commercial Li-ion full-cell systems.

Figure 3.1 shows the order of how the cells were assembled and this will be elaborated in the following. The cells were assembled inside a glove box with water and oxygen contents below 1 ppm. Before starting the cell assembly, electrodes of diameter 16 mm were cut and their thickness and mass were measured. A counter electrode of diameter 14 mm was cut from a 0.75 mm

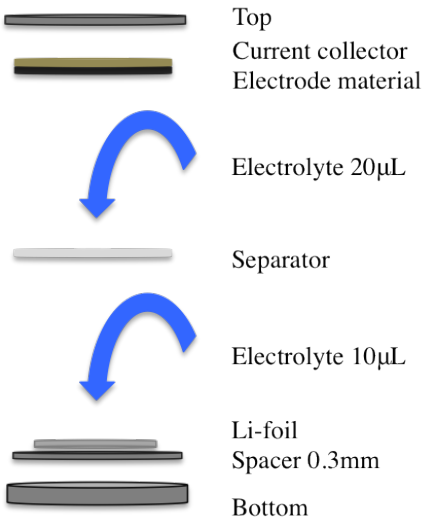

Figure 3.1: Cross sectional stacking order of a coin cell.

thick lithium foil (Alfa Aesar, 99.9 %). This was placed on a stainless steel spacer (CR 2016: SUS316L, Hohsen Corp.) of 0.3 mm and placed in the bottom case of the Hohsen cell with an inner isolating gasket. 10 μL of electrolyte was added onto the lithium foil and a 16 mm diameter 20 μm microporous trilayer membrane (PP/PE/PP) (Celgard ®2320) was placed on top directly after, to avoid evaporation of the electrolyte. Another 20 μL of electrolyte was added on top of the separator. The working electrode was then placed on top of the separator, with the active material facing the separator. Finally the cap of the Hohsen cell was placed on top and the cell was sealed in an automatic crimping machine (Hohsen Corp.). Table 3.7 gives a matrix of the cell combinations that have been studied in this thesis. The abbreviations will be used throughout the rest of this thesis.

Table 3.7: Matrix of cell combinations.

Active material	Conductive additive	Current collector	Electrolyte	Abbreviation
G8	Super P Li	Copper foil	E1	GNE
G8	Super P Li	Copper foil with carbon coating	E1	GCVD
G8	Super P Li	Copper foil	E2	GAR
$LiMn_2O_4$	AO-2	Aluminum foil	E1	LMO8
$LiMn_2O_4$	Super P Li	Aluminum foil	E1	LSP8

3.5 Chemical vapor deposition (CVD)

In this work, a thermal CVD instrument (Graphene Square) with H_2, CH_4, Ar and N_2 connected was used to grow thin layers of graphene/carbon onto copper foils. The chamber of the instrument is normally kept under vacuum and was purged with N_2 before placing the copper foils inside. Figure 3.2 shows a schematic of the a CVD deposition oven.

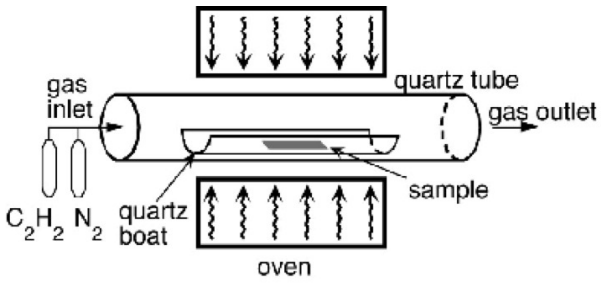

Figure 3.2: A schematic of a CVD deposition oven [56].

The growth process is illustrated graphically in Figure 3.3 and summarized in Table 3.8.

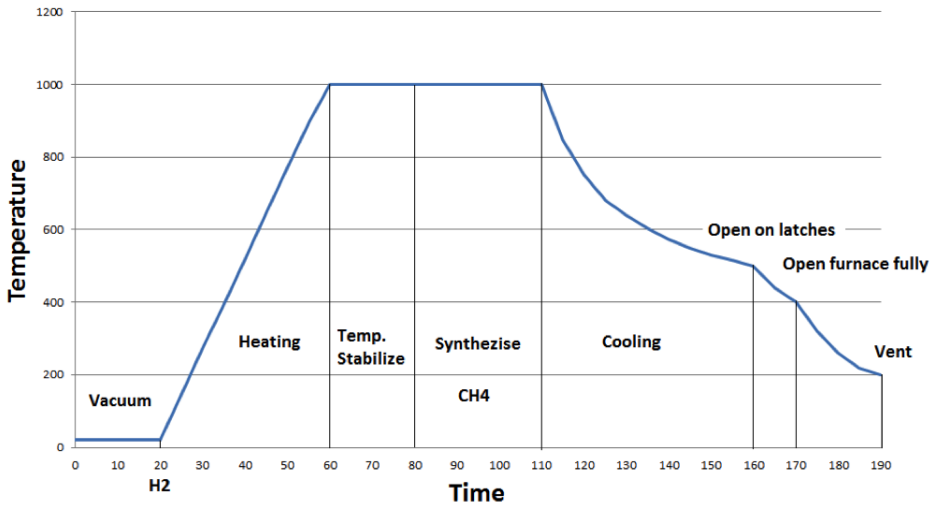

Figure 3.3: Graphical presentation of the carbon growth process in the CVD, showing the flow of gases and temperature changes. Modified from the user manual for the CVD instrument (Tool ID: 1462).

Table 3.8: Summery of the growth process of a carbon layer on copper foils. This table is modified from the user manual for the CVD instrument at NTNU NanoLab (Tool ID: 1462).

Time (Duration)	Step
Before program starts	Place copper foils inside the inner quartz tube and load into the chamber. Close and lock the furnace.
0 to 20 min (20 min)	Pump the chamber down to vacuum.
-	Flow 5 sccm H_2 into the chamber.
20 to 60 min (40 min)	Heat chamber from room temperature to 1000 °C at a temperature change rate of 25 °C/min.
60 to 80 min (20 min)	Temperature stabilizes at 1000 °C.
80 to 110 min (30 min)	Synthesis of graphene using 45 sccm CH_4. Adjust pressure to 5.0 torr .
110 to 160 min (50 min)	When temp $<$ 500 °C: Open furnace on latches with the lid hinged
170 min	Open the furnace lid fully
170 to 190 min (20 min)	When temp $<$ 200 °C the chamber can be vented

After venting the chamber, the samples were taken out and were ready to be used as current collectors. It was important to handle these foil as carefully as possible, since pre-washing with ethanol before casting could not be done in order to maintain the grown carbon layer.

3.6 Galvanostatic cycling

In this work, a computer controlled battery tester (Maccor, model 4200) was used for galvanostatic cycling of the coin cells. The reproducibility of the results was verified by making three coin cells of every cell composition. Two different cycling programs were made and used, one program for the coin cells with the negative electrode and one for the coin cells with the positive electrode. Varying charge and discharge rates (C-rates) were applied in the cycling programs. A current density of 1C is defined as the current required to completely charge or discharge a cell in one hour. For the negative and the positive electrode, the current density of 1C will hence be different due to difference in theoretical capacity. Calculations of the theoretical capacities are shown in Appendix A. The theoretical capacities for $LiMn_2O_4$ and graphite are 148 mAh/g and 372 mAh/g, respectively.

Cycling program of the negative electrode:

1 Initial galvanostatic discharge at 10mA/g (C/37) until 5mV.
2 Galvanostatic charge at a rate C/8 until 1.5V.
3 Three cycles between 1.5V and 5mV at a rate C/8.
4 Two cycles between 1.5V and 5mV at a rate C/2.
5 Two cycles between 1.5V and 5mV at a rate 1C.
6 Two cycles between 1.5V and 5mV at a rate 2C.
7 Two cycles between 1.5V and 5mV at a rate C/8.

Cycling program of the positive electrode:

1 Initial galvanostatic charge at 0.1C until 4.3V.
2 Galvanostatic discharge at 0.1C until 3V.
3 One cycle between 3V and 4.3V at a rate of 0.1C.
4 Five cycles between 3V and 4.3V at a rate of 0.5C.
5 Five cycles between 3V and 4.3V at a rate of 1C.
6 Five cycles between 3V and 4.3V at a rate of 2C.
7 Five cycles between 3V and 4.3V at a rate of 5C.

3.7 Characterization techniques

3.7.1 Raman spectroscopy

Raman measurements were performed by use of a confocal Horiba Jobin Yvon LabRAM HR 800 UV Raman microscope. The instrument was calibrated with a monocrystalline silicon sample before the measurements were performed. The laser used was a 30 mV 633 nm He-Ne laser. The confocal hole for the laser was set to 200 μm. The magnitude of the grating was 600. Acquisition time was set to 30 seconds with an accumulation number of 4.

Copper foil samples were placed on VWR microscope slides before placing it under the microscope objective for measurements. The carbon powders were pressed between two VWR microscope slides and the slide in which the powders sticked best were used for measurements.

Raman data processing

The spectra received from the measurements were baseline corrected with the Spec Lab 5 software from Horiba. The data were further processed by use of Kalman filter in MATLAB. The MATLAB code is given in Appendix B. The peak intensities I_D and I_G were acquired by direct readout in MATLAB.

3.7.2 Scanning electron microscopy (SEM)

The graphite powder, the conductive additive powders and the lithium metal oxide material were investigated by scanning electron microscopy (SEM, Zeiss Gemini Supra 55VP) in order to obtain information about the surface structures and particle sizes/shapes. The two different cathode casts were investigated in order to obtain information about the electrode morphology and the formation of the connecting network of conductive additives in the electrode. The lithium metal oxide powder and the cathode casts were gold sputter coated with an Edwards Sputter Coater S150B.The SEM was operated in secondary electron mode at 5 kV.

4. Results

In this chapter, results from particle size and -shape characterization, Raman spectroscopy measurements and electrochemical cycling will be presented in order. First, SEM images of the powders used for electrode preparation and the two different cathode cast will be presented. Raman spectra of the carbon conductive additive powders and copper foils with and without carbon coating are further provided. In the last section, results from electrochemical tests will be presented.

4.1 Scanning electron microscopy (SEM)

Investigation of the powders by SEM was conducted in order to verify technical properties (particle size and shapes) provided by the manufacturers. Table 4.1 lists the surface area, average particle size and capacity values of the powders used in the electrode manufacturing. These data are provided by the different manufacturers.

Table 4.1: Technical properties of materials used in electrode manufacturing.

Material	BET surface area [m^2/g]	Average particle size	Capacity [mAh/g]
CPreme®G8	< 2.3	7-10 μm	325
Carbon black	62[57]	40nm[57]	-
Grahene nanopowder	100[58]	~ 0.55 μm[58]	-
$LiMn_2O_4$	-	$<0.5\mu$m (BET)[59]	-

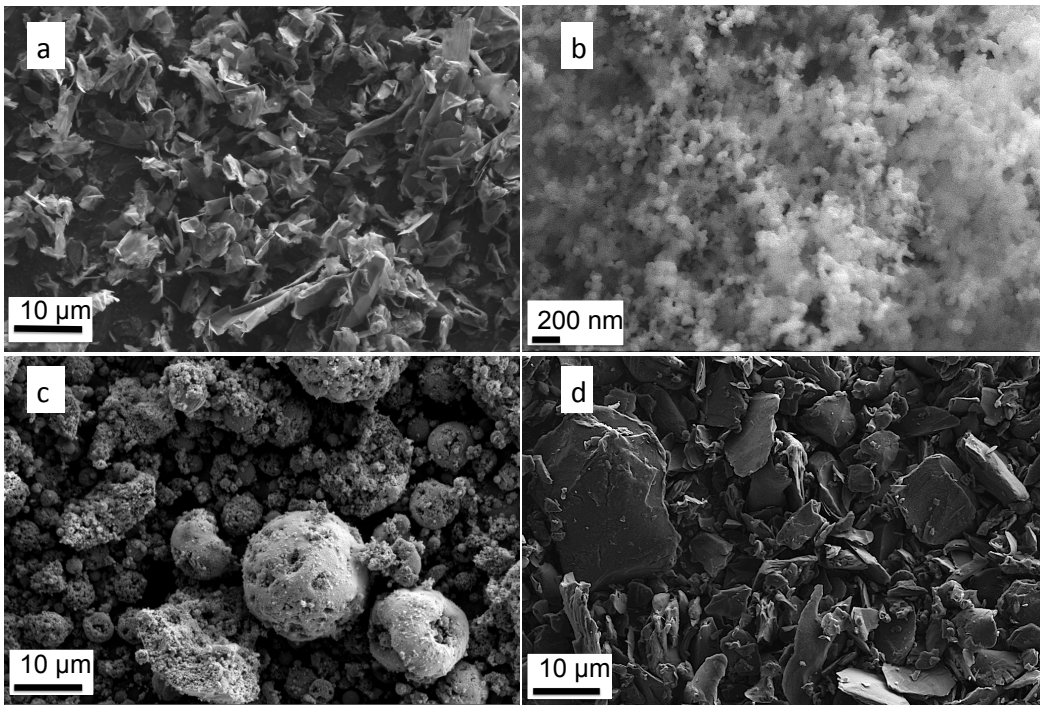

Figure 4.1: SEM images of the different powders used for electrode preparation. The picture shows the graphene nanopowder (AO-2) (a), carbon black (Super P Li) (b), gold sputtered lithium metal oxide ($LiMn_2O_4$) (c) and graphite (CPreme®G8) (d). The pictures were taken with the SEM operating in secondary electron mode at 5 kV, aperture in the range 20-30 μm and with working distances between 5.6 mm and 10.4 mm.

Figure 4.1 shows SEM images of the four powders used in the electrode manufacturing. In (a) the graphene nanopowder is depicted and in compliance with the product sheet the particle size is spanning over a wide range (150-3000 nm [58]). According to Figure 4.1(b) it seems that the particle size of carbon black is also in compliance with the manufacturers given value. The SEM image of the $LiMn_2O_4$ powder illustrates particles much greater than the particle size provided by the supplier and a broad particle size distribution. This might be due to agglomeration. The particle size of CPreme®G8 depicted in (d) also seems to be in accordance with the suppliers given value.

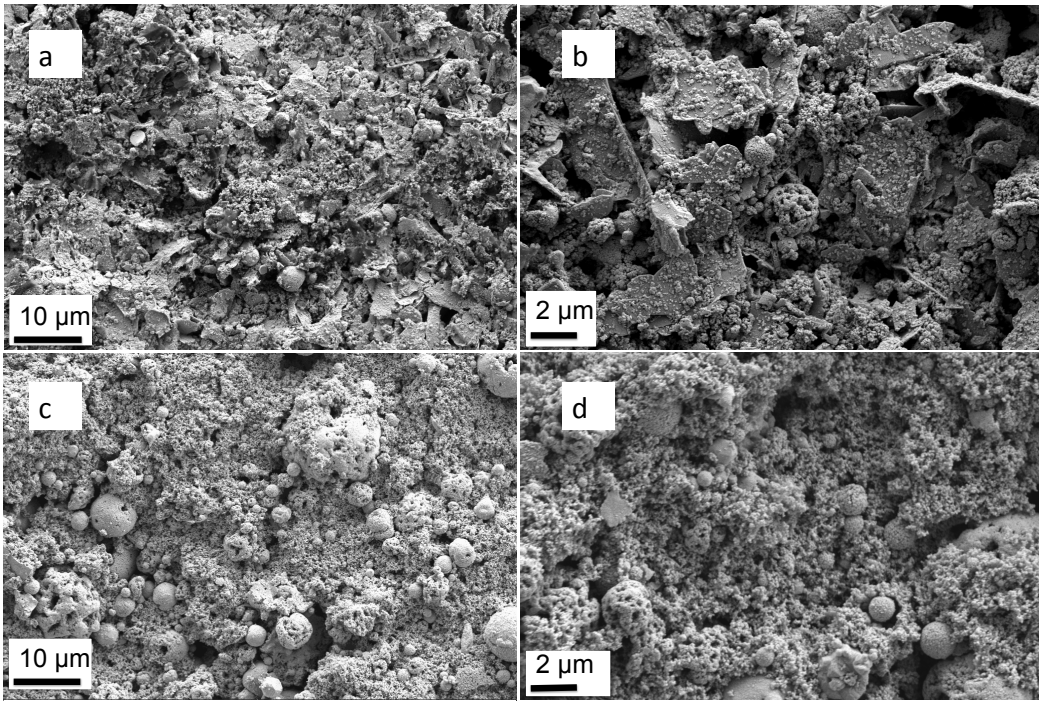

Figure 4.2: SEM pictures of the two different cathode cast used in this work. Picture (a) and (b) show the cast with graphene nanopowder as the conductive additive at different magnifications. Picture (c) and (d) show the cast with carbon black as the conductive additive at different magnifications. Both samples were gold sputtered before the pictures were taken. These pictures were taken with the SEM operating in secondary electron mode at 5 kV, aperture in the range 20-30 μm and with working distances between 5.9 mm and 6.1 mm.

Figure 4.2 show SEM images of the two different cathode casts. These pictures indicate a more porous and inhomogeneous resulting electrode for the cast with graphene nanopowder as conductive additive in comparison with the cast where carbon black is used as conductive additive.

4.2 Raman spectroscopy

Figure 4.3 shows the Raman spectra for a clean copper foil (a) and a copper foil with carbon layer (b) deposited by use of the Thermal CVD instrument at NTNU NanoLab. Figure 4.4 shows the Raman spectra for the two carbon powders used as conductive additives in electrode manufacturing, carbon black (a) and graphene nanopowder (b).

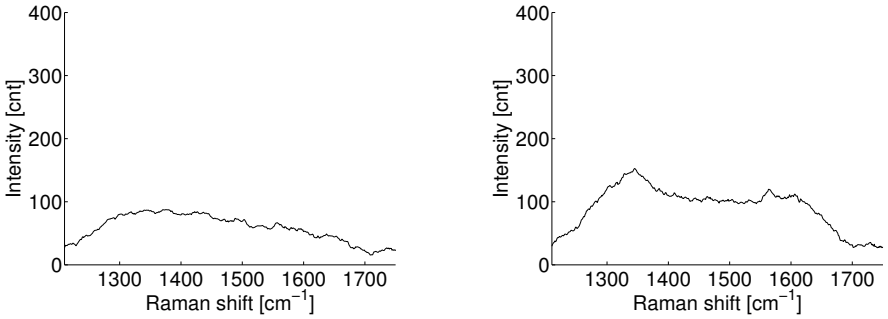

Figure 4.3: Raman spectra of a clean copper foil (a) and a copper foil with carbon layer deposited by CVD (b).

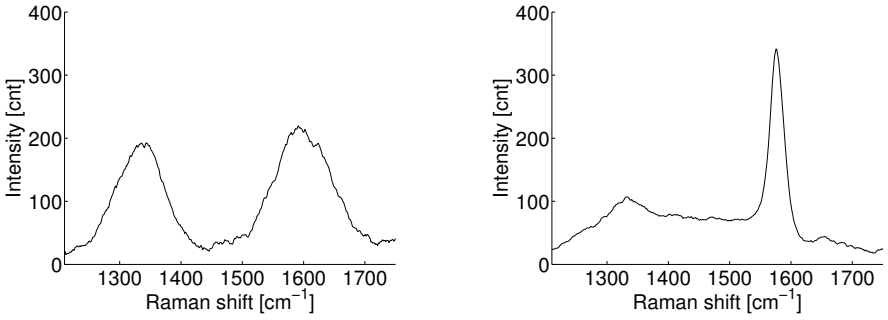

Figure 4.4: Raman spectra of the two carbon powders used as conductive additive in this work. (a) Carbon black and (b) graphene nanopowder.

As seen in Figure 4.3(b), small peaks are observed in the same areas as the D- and G peak of graphite/grahene occur. This indicates that carbon layer(s) have been deposited on the copper foil surface.

The spectra of the carbon conductive additives exhibit D-band and G-band

in approximately the same area as commercial graphite, with different intensities reflecting the difference in crystalline structure of the two powders. This is shown in Figure 4.4.

Table 4.2 gives the intensities of the D-peak and G-peak of the Raman spectra in Figure 4.4, and the particles crystalline size in basal direction, L_a, calculated by use of Equation 2.9. As there are considerable uncertainties in these measurements and the crystallite size in the basal direction, the values given in Table 4.2 should be considered as relative values rather than absolute values.

Table 4.2: Summary of intensity values of D-peaks and G-peaks, and L_a-values of the two conductive additives, carbon black and graphene nanopowder.

Material	Intensity of D peak	Intensity of G peak	L_a
Carbon black	192.7	219.4	110 Å
Graphene nanopowder	107	341.5	309 Å

4.3 Galvanostatic cycling

This section contains selected data from the electrochemical cycling of the different cell combinations, both anodes and cathodes. The main purpose of the electrochemical cycling was to investigate and compare the properties and performance of cells with different modifications conducted in terms of improving the rate capability.

4.3.1 Galvanostatic cycling of anodes made from CPreme® graphite.

Figure 4.5 shows the voltage-capacity curve of the initial discharge-charge cycle of one of the anode cells with electrode consisting of CPreme® graphite + carbon black (GNE #1). For the other Li/graphite half-cells used in this work the curves were similar. This figure illustrates the staged intercalation of lithium-ions into graphite as expected from theory.

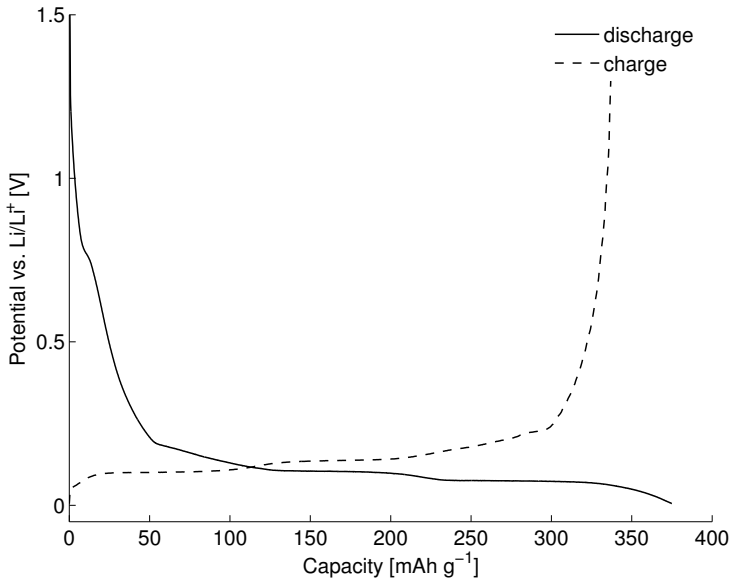

Figure 4.5: Voltage-capacity curve for the initial discharge-charge cycle of a the cell parallel GNE #1.

Figure 4.6 shows voltage-capacity curves at different current rates for the anode cell parallel GNE #1. As seen in this figure, all intercalation plateaus

are not shown for each cycle. The plot in Figure 4.6 indicates that complete intercalation of the graphite electrode did not take place at higher current rates.

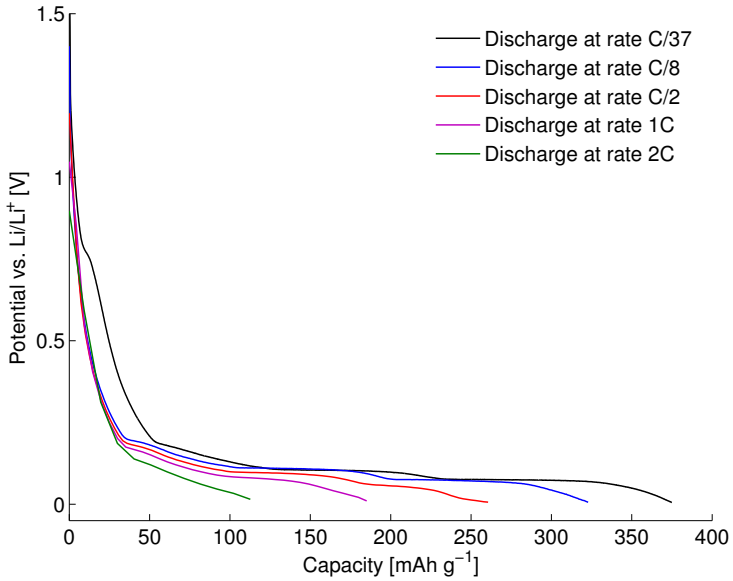

Figure 4.6: Voltage-capacity curves at different current rates for one anode cell with electrode consisting of CPreme® graphite + carbon black (GNE #1).

Table 4.3 lists the thickness and loading of each coin cell parallel.

Table 4.3: Summary of thickness and loading of the electrodes.

Cell combination	Sample number	Thickness [μm]	Loading of active material [mg/cm^2]
GNE	1	49	3.21
GNE	2	57.5	3.90
GNE	3	57	3.77
GCVD	1	49.5	3.17
GCVD	2	52	3.14
GCVD	3	52	3.01
GAR	1	56	4.09
GAR	2	55	3.82
GAR	3	52	3.50

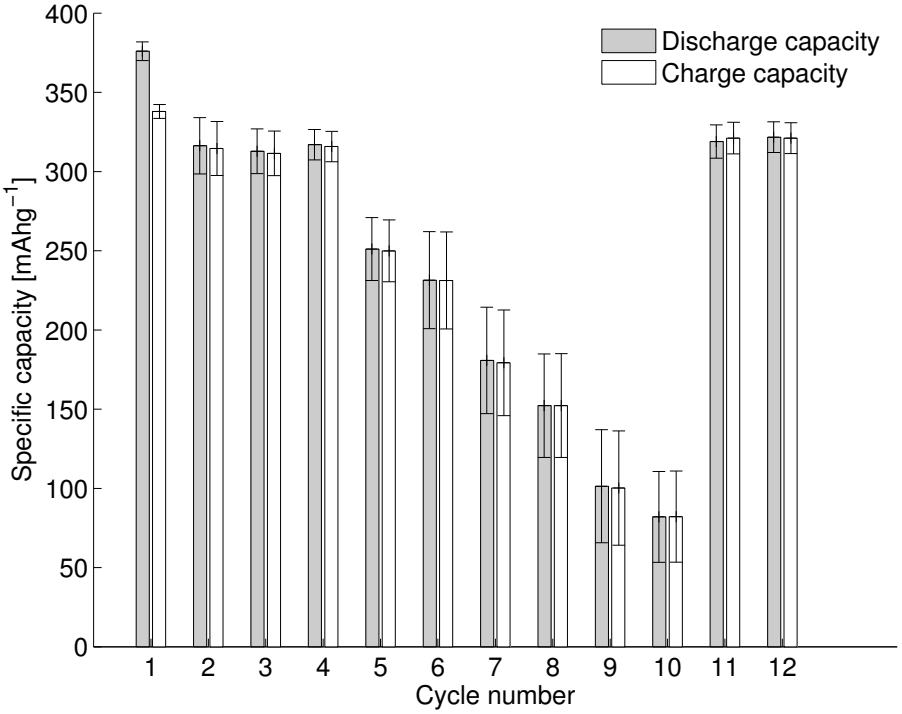

Figure 4.7: Average capacities with standard deviations for the three anode cells with electrode consisting of CPreme® graphite + carbon black.

Figure 4.7 displays the average capacities with standard deviations for the anode cells with electrode consisting of CPreme® graphite + carbon black (GNE), working as active material and conductive additive, respectively.

Figure 4.8 displays the average capacities with standard deviations for the anode cells with carbon coated current collector and electrode consisting of CPreme® graphite + carbon black (GCVD), working as active material and conductive additive, respectively.

Figure 4.9 displays the average capacities with standard deviations for the anode cells assembled by use of electrolyte E2 and electrode consisting of CPreme® graphite + carbon black (GAR), working as active material and conductive additive, respectively.

The height of the bars indicates the specific capacity for the discharging (grey) and charging (white) step of each cycle. Tables with capacity data for each parallel cell are given in Appendix C.1. Focusing on the operation at high current rates (2C rate, cycle 9 and 10), these results indicate that cells

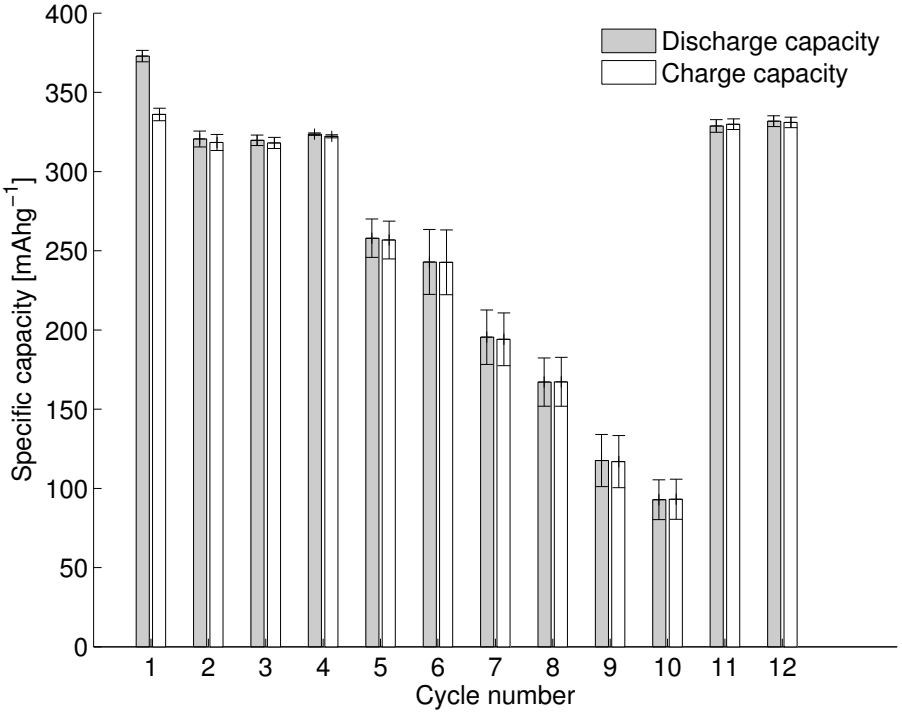

Figure 4.8: Average capacities with standard deviations for the three anode cells with carbon coated current collector and electrode consisting of CPreme® graphite + carbon black.

with carbon coated current collector achieve higher specific capacities than cells with uncoated current collectors, as can be observed from Figure 4.7 and Figure 4.8. By comparing Figure 4.7 and Figure 4.9, these results also indicate that cells assembled with electrolyte containing anion receptor (E2) achieved higher specific capacities than cells assembled with electrolyte not containing anion receptor (E1). The current program used to cycle anode cells is given in Section 3.6.

In Table 4.4 the irreversible capacity lost (ICL) for the first cycle are listed for every cell parallel.

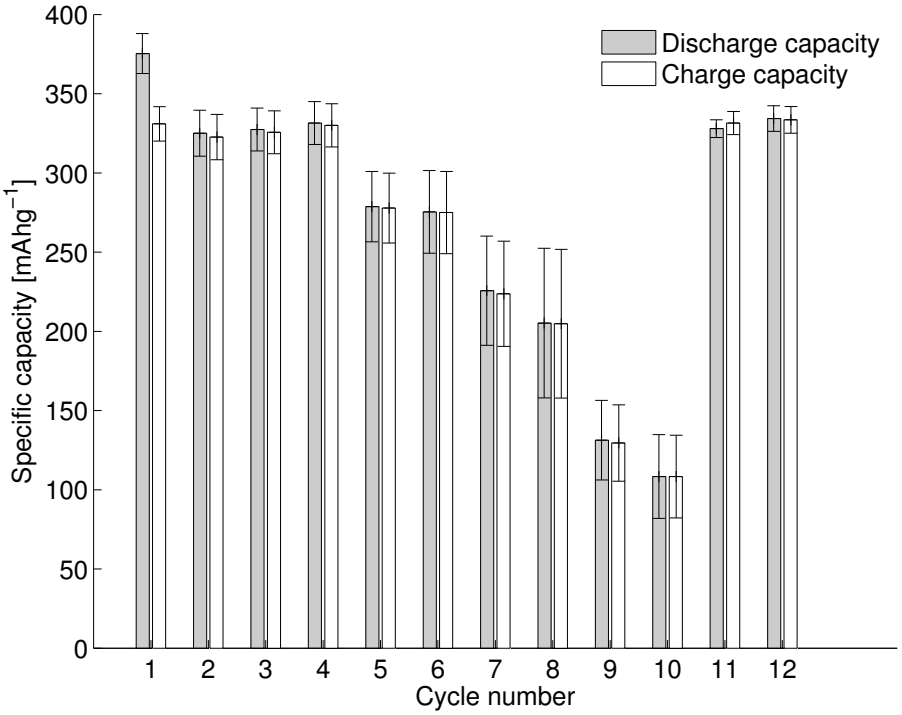

Figure 4.9: Average capacities with standard deviations for the three anode cells assembled with the use of electrolyte E2 and the electrode consisting of CPreme® graphite + carbon black.

Table 4.4: Performance characteristics of anode cells.

Cell combination	Sample number	ICL [%]
GNE	1	10.0
GNE	2	10.4
GNE	3	10.0
GCVD	1	9.7
GCVD	2	10.1
GCVD	3	9.8
GAR	1	12.8
GAR	2	11.2
GAR	3	11.5

4.3.2 Specific capacity values as a function of loading and thickness

Figure 4.10 and Figure 4.11 display capacity values at three different current rates for all anode cells as a function of loading of active material and electrode thickness, respectively. There is no clear relationship between neither capacity and loading nor capacity and electrode thickness, according to these figures.

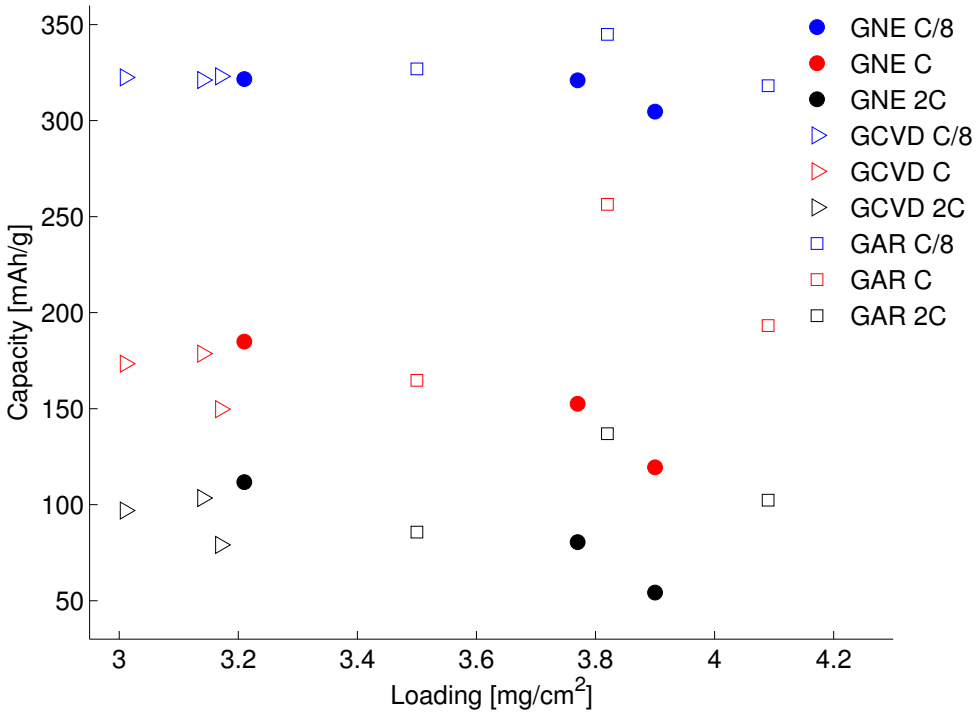

Figure 4.10: The capacity values at three different current rates for the anodes made from CPreme® graphite plotted against loading of active material in the electrodes. • points represent the cells with electrode consisting of CPreme® graphite + carbon black. ▷ points represent the anode cells with carbon coated current collector and electrode consisting of CPreme® graphite + carbon black. □ points represent the anode cells assembled by use of electrolyte E2 and electrode consisting of CPreme® graphite + carbon black.

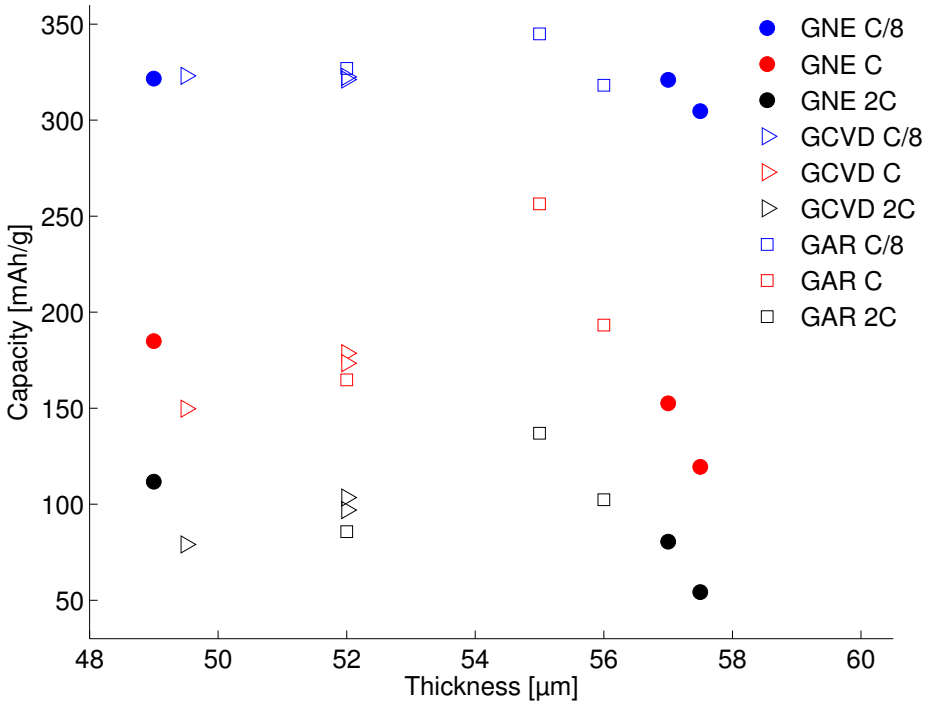

Figure 4.11: The capacity values at three different current rates for the for the anodes made from CPreme® graphite plotted against the thickness of the electrodes. • points represent the cells with electrode consisting of CPreme® graphite + carbon black. ▷ points represent the anode cells with carbon coated current collector and electrode consisting of CPreme® graphite + carbon black. □ points represent the anode cells assembled by use of electrolyte E2 and electrode consisting of CPreme® graphite + carbon black.

4.3.3 Study of overpotential in first and second cycle of cells with and without anion receptor added to the electrolyte

Differential capacity curves allow for precise determination of the intercalation potential at the various stages. Figure 4.12 displays the differential capacity values as a function of the cell potential (vs. Li/Li^+) for the first and second cycle of the cell parallel GNE #2 (anode cell assembled with electrolyte E1). Figure 4.13 displays the differential capacity values as a function of the cell potential (vs. Li/Li^+) for the first and second cycle of the cell parallel GAR #1 (anode cell assembled with electrolyte E2).

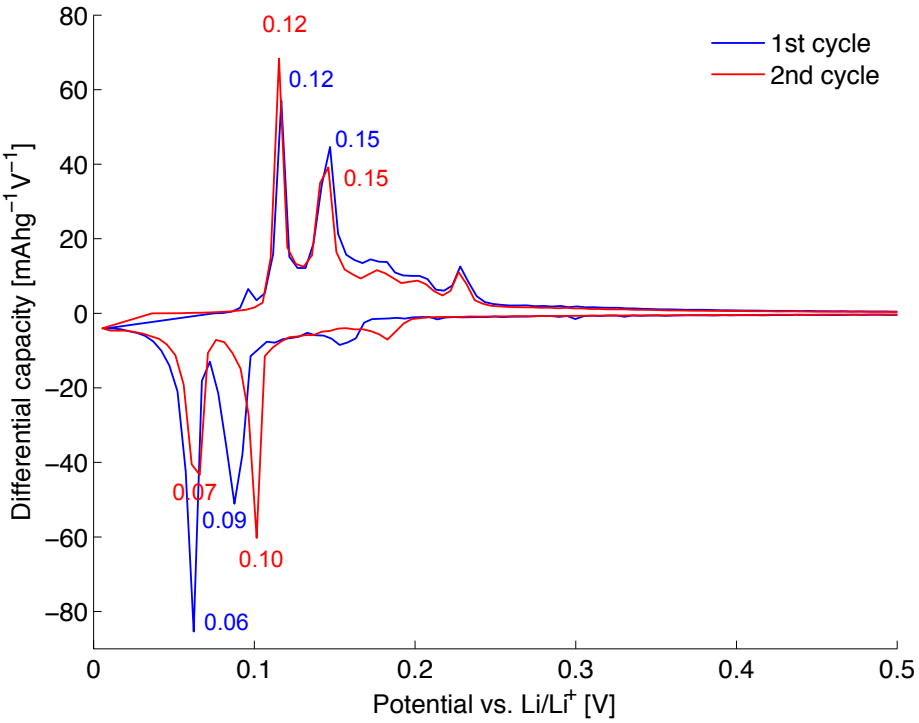

Figure 4.12: Differential capacity values plotted as a function of the cell potential (vs. Li/Li^+) for the first and second cycle for the cell parallel GNE #2.

Unfortunately, the differential capacity curves shown in Figure 4.12 and 4.13 are the only ones available due to a computer crash after a low of power in the building.

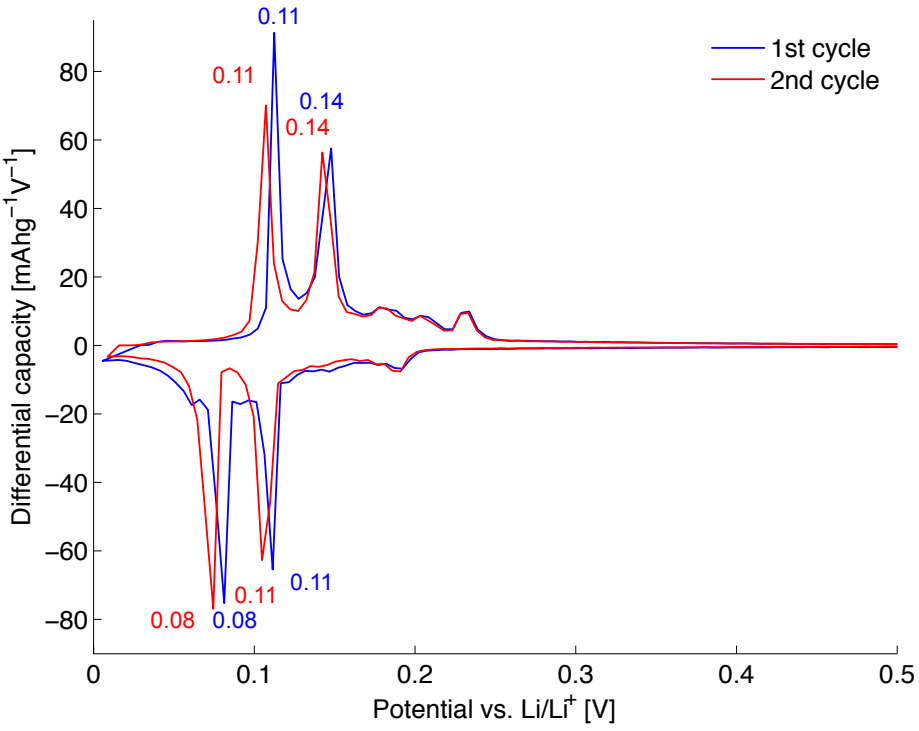

Figure 4.13: Differential capacity values plotted as a function of the cell potential (vs. Li/Li$^+$) for the first and second cycle for the cell parallel GAR #1.

4.3.4 Galvanostatic cycling of cathodes made from lithium manganese oxide ($LiMn_2O_4$).

Figure 4.14 displays the average capacities with standard deviations for the cathode cells with electrode consisting of lithium manganese oxide + graphene nanopowder (LMO8), working as active material and conductive additive, respectively. Figure 4.15 displays the average capacities with standard deviations for the cathode cells with electrode consisting of lithium manganese oxide + carbon black (LSP8), working as active material and conductive additive, respectively.

The height of the bars indicates the specific capacity for the charging (white) and discharging (grey) step of each cycle. Tables with data for each parallel cell is given in Appendix C.2. These average data plots indicate that cathode cells with carbon black used as conductive additive withstand high current rates substantially better than cells were the graphene nanopowder was used as conductive additive.

The current program used to cycle cathode cells is given in Section 3.6. In addition, one cell with electrode consisting of lithium manganese oxide + graphene nanopowder was cycled with five (instead of two) initial cycles at low current (14.8 mAg^{-1}) and in addition, five more cycles at low current rate (14.8 mAg^{-1}) at the end of the given current program. Note that this cell was not made from the same electrode cast as the three parallels in Figure 4.14. However, this electrode cast was made by the same recipe as given in Table 3.4 and hence, it should be comparable. Table 4.5 gives the thickness and loading of each coin cell parallel .

As Figure 4.16 shows, the cell is not damaged by high currents, as the capacities are approximately preserved when the cell again are cycled at low currents.

Table 4.5: Summary of thickness and loading of the electrodes.

Cell combination	Sample number	Thickness [μm]	Loading of active material [mg/cm^2]
LMO8	1	51-53	1.99
LMO8	2	48-50	1.83
LMO8	3	57-62	2.68
LSP8	1	57-58	1.85
LSP8	2	61-65	2.62
LSP8	3	61-63	2.33

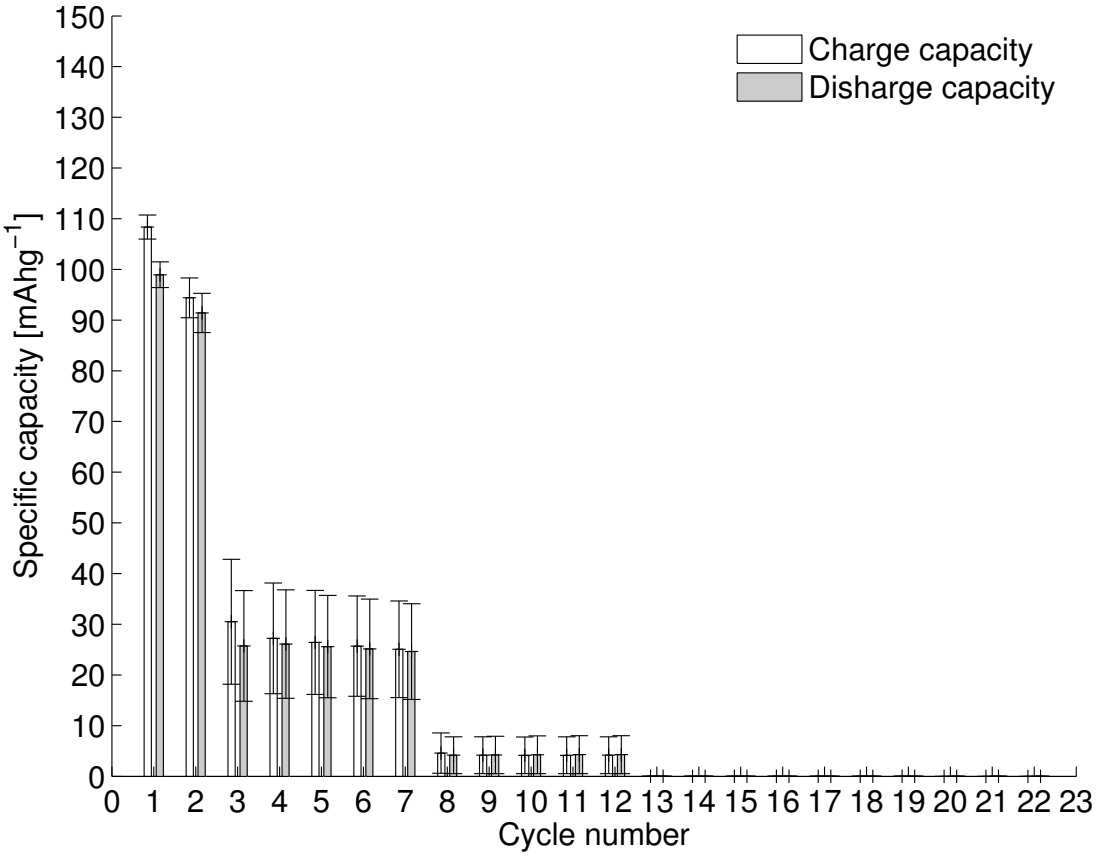

Figure 4.14: Average capacities with standard deviations for the three cathode cells with electrode consisting of lithium manganese oxide ($LiMn_2O_4$) + graphene nanopowder (AO-2).

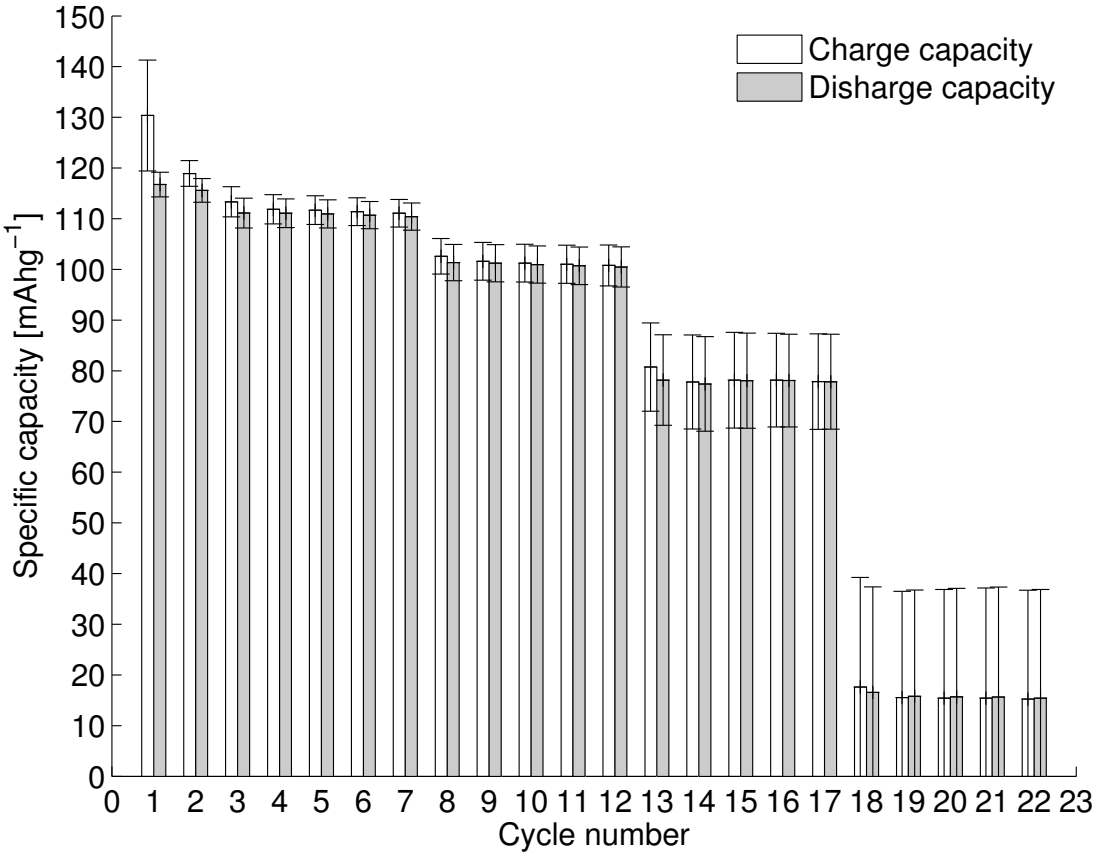

Figure 4.15: Average capacities with standard deviations for the three cathode cells with electrode consisting of lithium manganese oxide ($LiMn_2O_4$) + carbon black (Super P Li).

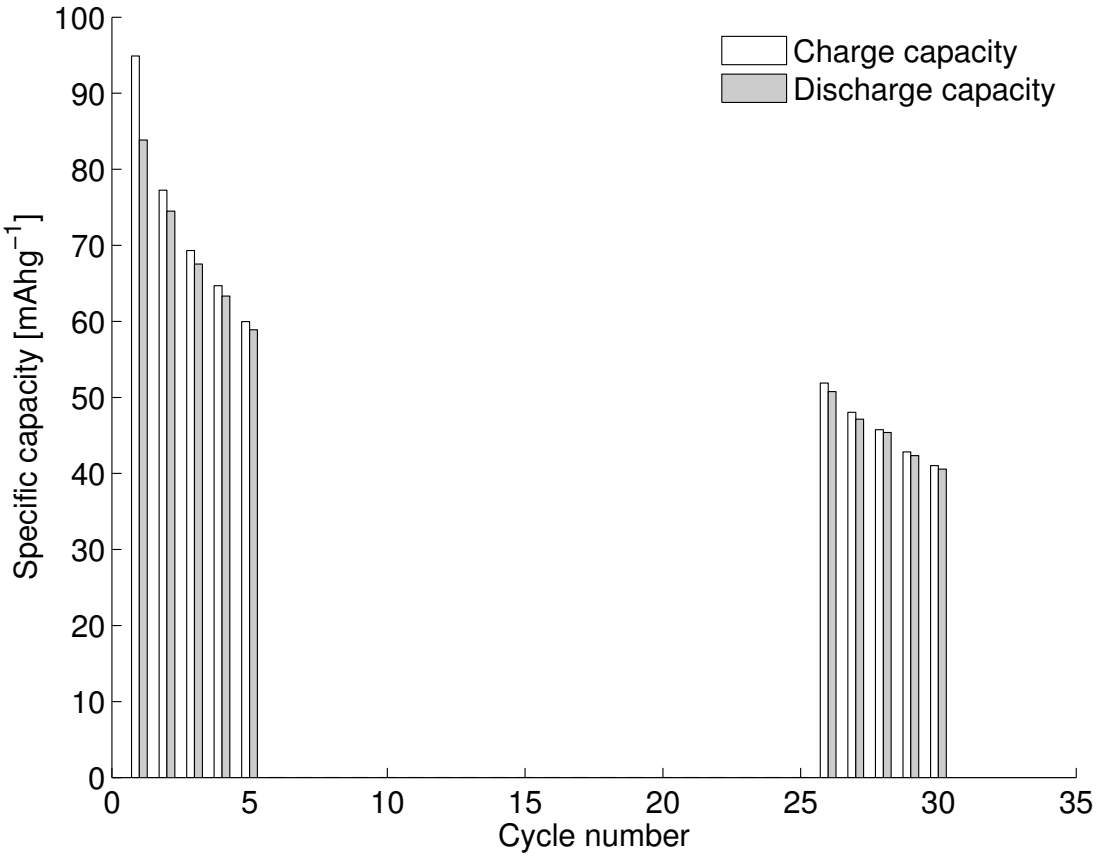

Figure 4.16: Capacities of one cell with electrode consisting of Lithium manganese oxide ($LiMn_2O_4$) + graphene nanopowder (AO-2).

5. Discussion

This discussion will mainly focus on the results and findings obtained regarding the three different modifications performed in order to improve the rate capability of lithium-ion electrodes. The results obtained from SEM and Raman spectroscopy will be used as supplement to explain electrochemical behavior and thus, these results will not be discussed independently.

Figure 4.6 displays voltage-capacity curves at different current rates for one anode cell with electrode consisting of CPreme® graphite + carbon black (GNE #1). As all anode cells cycled in this work showed similar trends with increasing current rates, only one plot is included to illustrate this trend. The figure shows that the capacity of the cell decreases with increasing current rates. This capacity loss can be ascribed to the incomplete intercalation of Li-ions in the graphite electrode at high rates. With increasing current rates, a voltage gradient will build up and the inner of the electrode material will not be utilized. Hence, the thickness of the electrode is a key property in the optimization of battery performance.

Reduction of interfacial contact resistivity between the active layer and current collector

The short guide manual provided for the thermal CVD instrument at NTNU NanoLab was used for graphene growth on current collectors in this work. The short guide uses a standard graphene on copper growth recipe for all parameter examples. Figure 4.3(b) shows the Raman spectrum of the copper foil with carbon layer. The spectrum displays a slight peak at ~ 1350 cm^{-1}. According to theory, this peak indicates that the graphene layer is not free of defects.

Unfortunately, as clearly seen from the Raman results, this process did not give a resulting graphene layer on the copper surface. Detection of a thin carbon layer on the surface was made, but the resulting peak intensities in the Raman spectrum of this layer indicates that it is a thin carbon layer with a considerable fraction of edge/defect sites, and is thus not a graphene layer.

According to literature [43, 45], rate performance of Li-ion electrodes exhibit remarkable enhancement when aluminum and copper current collectors are coated with carbon by a chemical vapor deposition process. By comparing the average capacities of cells with and without coated current collectors, as illustrated in Figure 4.8 and Figure 4.7, it seems that the obtained capacities are slightly enhanced for the cells with coated current collectors. However, it is worth noting that there are significant error bars in these bar plots, indicating that there are considerable variations among the different parallels with the same cell combination. Thus, more parallels are needed to confirm this result. Also, differences in loading, thickness and porosity will influence on the results.

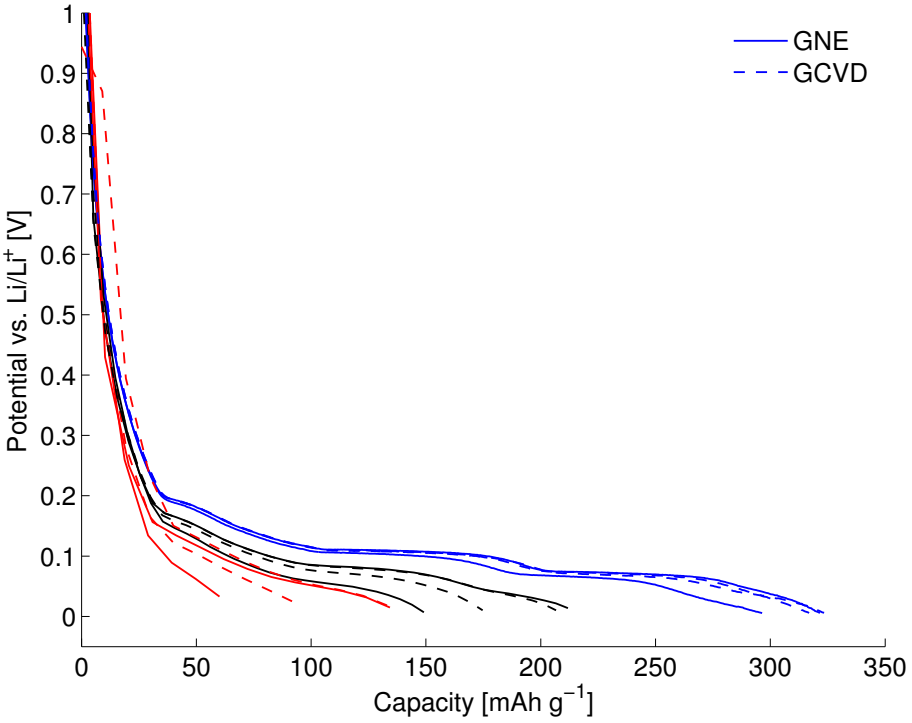

Figure 5.1: Discharge voltage curves. Solid lines represent GNE cells (parallel 1 and 2) and the dashed lines represent GCVD cells (parallel 1 and 2). The different colors represent different current rates (— = 46.5 mAg^{-1}, — = 372 mAg^{-1}, — = 744 mAg^{-1}.)

For illustration of the differences among the various cells, two additional plots are displayed. Figure 5.1 shows the discharge voltage curves of four anode cells (two with and two without carbon coated current collector). Unlike the

average capacity plots, this plot do not clearly indicate that coating of current collector enhances cell performance. As outlined in Section 3.1, discharge of Li/graphite half-cells means lithium intercalation into the graphite electrode and hence, this plot illustrates the charge characteristics of the graphite electrodes in a full-cell systems. Charge characteristics provides important information, as ability to reversibly intercalate lithium at high rates would be very attractive with regards to use in electric vehicles, as this would be beneficial for faster charge [36].

Figure 5.2 shows the charge voltage curves of the same four anode cells displayed in Figure 5.1. As charge curves illustrate de-intercalation of the graphite electrode in Li/graphite half-cell systems, this shows how the electrodes would perform during operation (upon discharge) in a full-cell system. Not even in this plot is there a clear indication of enhanced performance for cells with coated current collector. However, Figure 4.10 and Figure 4.11 might help enlighten the observed results.

As seen in Figure 4.10 there is no a clear relationship between loading and specific capacity for the cells with coated current collector. However, for the cells with uncoated current collector, there might be a slight trend showing that the capacities are lowered with increasing loading. Figure 4.11 also shows a slightly decreasing trend for the cells with uncoated current collector with increasing thickness. This trend might be related to incomplete intercalation of the thicker electrodes and is not observed for the cells with coating since these are considerably thinner and has lower loading than the GNE cells.

Hence, as Figure 4.10 and Figure 4.11 show, there are no clear correlations and therefore, more cells are highly necessary in order to understand the effect of coating. More detailed studies of the coating itself should also be performed.

Uncertainty in the above results might also be related to quality of the active layer and the adhesion between the electrode material and the current collector. As the coated copper foil was curved in the tube upon the thermal chemical vapor deposition process, this foil was not as smooth as the uncoated copper foil. The rougher surface may have resulted in poorer quality (homogeneity) and adhesion and hence, no overall reduction of interfacial resistance between the current collector and active layer.

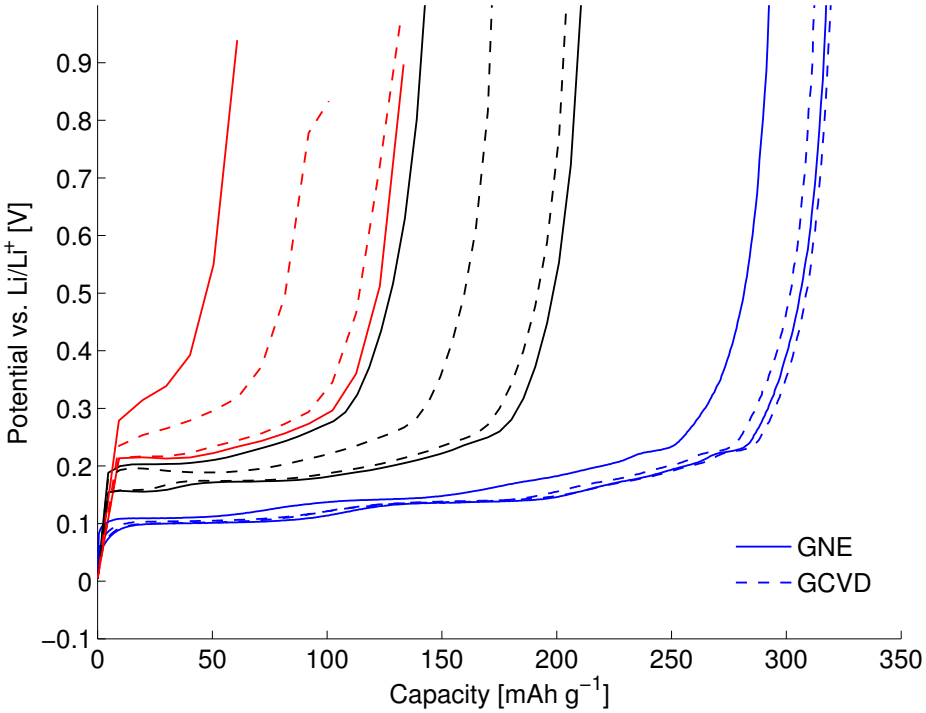

Figure 5.2: Charge voltage curves. Solid lines represent GNE cells (parallel 1 and 2) and the dashed lines represent GCVD cells (parallel 1 and 2). The different colors represent different current rates (— = 46.5 mAg^{-1}, — = 372 mAg^{-1}, — = 744 mAg^{-1}.)

Replacement of carbon black by graphite/graphene as conductive additive in cathode.

As previously elaborated in Section 2.6.2, graphene has an extremely high surface/mass ratio, and its structure assures one of the highest electron conductivities [2]. Considering this clearly advantageously property, one would expect graphene to be a better choice for use as conductive additive in cathode materials. However, the results achieved in this work do not provide the improvement expected for this replacement.

As Figure 4.14 and Figure 4.15 in Section 4.3.4 show, replacement of carbon black by the graphene nanopowder did not result in enhancement of capacity values for the cathodes tested. In fact, the obtained results indicate that the cells with graphene nanopowder as conductive additive do not withstand

high current rates. As outlined earlier in the theory, the role of the conductive additive is to enhance the electrode conductivity by filling the free spaces made by the grains of active material to form a continuous network. Hence, a homogeneous dispersion of the active material and conductive additive throughout the electrode is important because the cell polarization and utilization of active material is determined by this feature.

Particle size and shape, density, volume fraction of individual components, and inter-particle interaction forces are all important parameters affecting the ability of homogenous dispersion of the different components throughout the electrode. Figure 4.2(a) and (b) display SEM images of the cathode cast where graphene nanopowder is used as conductive additive, while Figure 4.2(c) and (d) present the cast where carbon black is used as conductive additive. The images show a more porous structure for the electrode with graphene nanopowder. A possible explanation for a more porous resulting electrode by change of conductive additive might be ascribed to the particles size and shape. The graphene nanopowder show a large range of particle sizes and shapes, as seen in Figure 4.1 (a). The carbon black particles seem to have a more homogenous particle size and shape distribution. The difference in particle size and shape between the graphene nanopowder and the active material, shown in Figure 4.1 (c), is small compared to the difference in particle size and shape between the carbon black and the active material. The carbon black might therefore be able to fill smaller pores throughout the electrode and be distributed more evenly and create a better continuous electrical network within the electrode, resulting in better cycleability of the electrode.

Another aspect to be considered is the importance of the quality of the graphene nanopowder. Figure 4.4(b) shows the Raman spectrum of the graphene nanopowder. From Raman measurements it turned out that the graphene nanopowder (AO-2, Graphene supermarket) is not graphene, but a multilayer graphite-like powder, with a wide particle size distribution and an interlayer spacing close to graphite .

The cell in Figure 4.16 have been cycled with the following current program:

1 Five cycles between 3V and 4.3V at a rate of 0.1C.
2 Five cycles between 3V and 4.3V at a rate of 0.5C.
3 Five cycles between 3V and 4.3V at a rate of 1C.
4 Five cycles between 3V and 4.3V at a rate of 2C.
5 Five cycles between 3V and 4.3V at a rate of 5C.
6 Five cycles between 3V and 4.3V at a rate of 0.1C.

As the figure displays, this cast shows a very low rate capability, as the capacities approach zero after only the first five cycles. But, it also shows that the cell is exhibiting significant capacity values when the cell again is cycled at low current rate. This result implies that the cell is not destroyed upon high current rates, but that the rate capability of this cell is rather poor.

Modification of electrolyte

By comparing the average capacities of cells assembled with different electrolytes, as illustrated in Figure 4.7 and Figure 4.9 it seems that the obtained capacities are increased for the cells containing anion receptor. As for the capacity values of the cells with coated current collector, it is worth noting that there are significant error bars in these bar plots, which implies that there is considerable variation between the different parallel cells. A complete overview of all capacity data is given in Appendix C.

Figure 4.12 and Figure 4.13 display the differential capacity values as a function of the cell potential (vs. Li/Li^+) for the first and second cycle of the cell parallel GNE #2 (Anode cell assembled with electrolyte E1) and GAR #1 (Anode cell assembled with electrolyte E2), respectively.

Some key results can be seen from these two plots:

1. The overpotential in the first cycle intercalation is lower in the cell assembled with electrolyte E2.
2. In the cell assembled with electrolyte E2, overpotentials are equal in the first and second cycle.
3. By comparing the two cells it is seen that overpotentials for both intercalation and de-intercalation is consistently lower for the cell containing anion receptor.

As these results are based upon just one cell for each cell combination, it can

not be stated that these results are valid for all parallels. However, based on these results, it seems that the addition of anion receptor helps lowering overpotentials in the cell associated with intercalation and de-intercalation. The overlap of the differential capacities for the first and second cycle in the cell containing anion receptor, as displayed in Figure 4.13, indicates that the overpotential associated with SEI formation in the first cycle is reduced when anion receptor is present in the electrolyte.

6. Conclusion

Various methods to improve the rate capability of Li-ion electrodes were investigated in this work. These methods include improving the electronically conducting network of the electrodes by reducing the interfacial contact resistivity to the current collector, replacing the carbon black conductive additive by graphite/graphene, as well as reducing the resistance related to intercalation of lithium-ions into the graphite particles by addition of anion receptor in the electrolyte.

Based on average capacity values, it appears that the cells with carbon coated current collector have demonstrated higher capacities and improved rate capabilities compared to cells without coating. However, due to variation in thickness and loading among parallels with the same cell combination, significant individual differences in performance between cells of equal cell combination have been observed. Hence, based on these results the concluding remark is that more parallel experiments are necessary in order to obtain a reliable conclusion regarding the effect of the coating.

Based on average capacity values for cells assembled with different electrolytes, it seems that the obtained capacities are increased for the cells containing anion receptor. Differential capacity data also indicate that the overpotential associated with SEI formation in the first cycle is reduced with presence of anion receptor in the electrolyte and that it helps lowering overpotentials in the cell associated with intercalation and de-intercalation. Unfortunately, these latter results are only based on one cell for each electrolyte, and more data should be accessible in order to confirm these observations.

For the cathode cells, replacement of carbon black by grapheme nanopowder did not improve the cell performance. From particle size and shapes detected by SEM for the conductive additives and the active material, there is clear that graphene nanopowder would be less able to create a continuous conducting network within the electrode than the carbon black. Raman measurements also showed that the graphene nanopowder was not perfect graphene, but likely somewhat more similar to graphite.

7. Further work

Coating of current collectors

As the Thermal CVD instrument was newly installed at NTNU NanoLab at the time I started this thesis, only one temperature program was tested for graphene growth on copper foils. As seen in literature, other temperatures and durations have been applied, and further work could be to attempt optimize the temperature program for graphene growth.

Another issue regarding the Thermal CVD instrument is the size and shape of the sample holder. The cylindrical quartz tube holder for samples have a diameter of 1.5 inches, making it difficult to prevent the copper foil from become wrinkled during the deposition process. An idea for further work could be to invest in a new sample holder that allows the copper foil to be in a flat position throughout the deposition process.

This June (2014) there will be installed a Raman spectroscope at NTNU NanoLab. For more precise characterization of the deposited carbon layer from the Thermal CVD processes, an idea for further work could be to use this new instrument for characterization of coatings.

Another idea for further work could be coating of aluminum foils for use as current collectors. As Al has its melting point at 660°C, it requires another temperature program than the one used for the copper foil. An attempt was made to grow graphene on aluminum foils in this work, but characterization by Raman did not indicate that a carbon layer had been formed. Thus, this aluminum foil was not used in the further work performed.

Conductive additives in cathode preparation

The quality and features of graphenes/graphites for use as conductive additive in electrode preparations are of great importance for the electrode performance. Hence, characterization of these carbons will always be essential for understanding of the electrode behavior.

Electrolyte additives

Use of the anion receptor tris(hexafluoroisopropoyl) borane (THFIPB) showed promising results in this work. Hence, further investigation with various carbons and electrolyte compositions should be made.

Appendix A

A.1 Calculation of theoretical capacities for the active materials

Faraday´s 1st law of electrochemistry states that 1 gram equivalent weight of a material will deliver 96487 coulombs (or 26.8 Ah). A gram-equivalent weight is the atomic or molecular weight of the active material in grams divided by the number of electrons involved in the reaction. The theoretical capacities of the graphite material and the lithium metal oxide can hence be calculated easily from this law. For $LiMn_2O_4$ the equivalent weight is 180.8 g/mol, giving a theoretical capacity of [60] :

$$\frac{26.8\text{Ah/mol}}{180.8\text{g/mol}} = \underline{148\text{mAh/g}}$$

We know from the theory that the final structure of the intercalated graphite has the formula LiC_6. The theoretical capacity of this structure can thus be calculated as follows:

Moles of carbon atoms per gram graphite:

$$n_{\text{C}} = \frac{1\text{g}}{12.01\text{g/mol}} = 0.0833\text{mol}$$

Moles of Li^+ per gram graphite:

$$n_{\text{Li}^+} = \frac{n_{\text{C}}}{6} = 0.0139\text{mol}$$

This implies that the equivalent weight of Li^+ in this structure is 1/0.0139 = 71.9g/mol

Theoretical capacity of the graphite structure is hence:

$$\frac{26.8\text{Ah/mol}}{71.9\text{g/mol}} = \underline{372\text{mAh/g}}$$

Appendix B

B.1 MATLAB code for processing of Raman results

This appendix gives the MATLAB code for the filter applied to the results achieved from the Raman spectroscope measurements. The script `ramanfilter.m` plots the Raman spectrum and make use of `KalmanFilt_h.m` to smooth the curve. Preparation of the `KalmanFilt_h.m` code was done by others that has been acknowledged.

`ramanfilter.m` :

```
data  = load('datafil.txt');

x = data(:,1);
y = data(:,2);

yk = KalmanFilt_h(y);
yk = yk(1,:);
plot(x,yk,'b', 'LineWidth',1)
xlabel('Raman shift [cm^-^1]')
ylabel('Intensity [cnt]');
```

KalmanFilt_h.m :

```
function [ H_est] = KalmanFilt_h( h_inp )

    A_c = [0,1;0,0];
    E_c = [0;1];

    [A_d,E] = c2d(A_c,E_c,1/30);
    H = [1,0];

    H_est = zeros(2,max(size(h_inp)));
    H_est(1,1) = h_inp(1);
    P_pred = [100,0;0,1000];
    H_pred = H_est(:,1);

    sigma_w_h = 800e-6;
    sigma_r_h = 2e-5;

    for i = 2:max(size(h_inp))
        K_k = P_pred*H'*inv(H*P_pred*H'+sigma_r_h);
        H_est(:,i) = H_pred + K_k*(h_inp(i)-H*H_pred);
        P_hat = (eye(2)-K_k*H)*P_pred*(eye(2)-K_k*H)'
                + K_k*sigma_r_h*K_k';

        H_pred = A_d*H_est(:,i);
        P_pred = A_d*P_hat*A_d' + E*sigma_w_h*E';
    end

end
```

Appendix C

C.1 Capacity values obtained for anodes made from CPreme® graphite

Table C.1 - C.3 lists all capacity data obtained from cycling of anodes made from CPreme® graphite.

Table C.1: Capacity values for the three anode cells with electrode consisting of CPreme® graphite + carbon black.

	GNE4		GNE2		GNE3	
Cycle no.	Charge cap. [mAh/g]	Discharge cap. [mAh/g]	Charge cap. [mAh/g]	Discharge cap. [mAh/g]	Charge cap. [mAh/g]	Discharge cap. [mAh/g]
1	337.60	374.93	333.66	370.64	342.40	382.31
2	319.35	321.34	295.63	296.56	328.72	330.94
3	319.84	321.24	295.26	296.54	319.33	320.74
4	321.65	322.87	304.72	305.89	321.01	322.15
5	264.23	265.82	227.73	228.47	257.86	258.85
6	260.36	260.59	199.31	199.57	234.00	234.19
7	213.48	215.42	146.77	148.34	177.54	178.50
8	184.92	184.63	119.42	119.37	152.52	152.57
9	137.44	138.23	65.47	66.99	97.72	98.81
10	111.75	111.44	54.24	54.16	80.51	80.44
11	323.80	321.41	310.10	307.43	329.49	328.04
12	325.61	326.12	309.92	310.57	327.80	328.42

Table C.2: Capacity values for the three anode cells with carbon coated current collector and electrode consisting of CPreme® graphite + carbon black.

	GCVD1		GCVD2		GCVD3	
Cycle no.	Charge cap. [mAh/g]	Discharge cap. [mAh/g]	Charge cap. [mAh/g]	Discharge cap. [mAh/g]	Charge cap. [mAh/g]	Discharge cap. [mAh/g]
1	340.25	376.76	332.42	369.62	335.55	372.21
2	323.99	326.19	314.21	316.61	316.79	318.87
3	321.76	323.27	314.86	316.78	317.52	319.11
4	323.07	324.35	321.18	322.78	322.50	323.78
5	245.64	246.42	269.39	270.60	255.33	256.71
6	219.35	219.53	257.51	257.87	251.13	251.41
7	175.46	176.24	207.57	209.31	199.33	200.73
8	149.73	149.73	178.65	178.31	173.42	173.30
9	98.62	99.33	130.65	131.41	121.40	121.97
10	79.00	78.84	103.48	103.12	96.97	96.64
11	333.75	333.33	327.57	326.22	328.35	326.72
12	334.77	335.71	328.64	329.46	329.63	330.14

Table C.3: Capacity values for the three anode cells assembled by use of electrolyte E2 and the electrode consisting of CPreme® graphite + carbon black.

	GAR1		GAR2		GAR3	
Cycle no. [mAh/g]	Charge cap. [mAh/g]	Discharge cap. [mAh/g]	Charge cap. [mAh/g]	Discharge cap. [mAh/g]	Charge cap. [mAh/g]	Discharge cap.
1	332.69	381.47	340.87	383.72	319.40	360.90
2	322.12	324.98	337.21	339.63	308.62	310.61
3	318.06	320.08	341.23	342.98	317.67	319.10
4	318.19	319.90	344.97	346.39	326.95	328.17
5	273.55	274.57	301.68	302.75	258.18	258.90
6	267.54	267.95	303.87	304.42	253.63	253.89
7	207.23	209.08	261.92	265.28	202.03	202.63
8	193.28	193.62	256.42	257.14	164.77	164.83
9	119.18	120.48	157.07	160.04	112.27	113.42
10	102.31	101.80	136.95	137.47	85.72	85.83
11	323.49	321.50	337.84	330.67	333.14	331.68
12	323.93	325.11	339.67	340.34	336.98	337.44

C.2 Capacity values obtained for cathodes made from lithium manganese oxide ($LiMn_2O_4$)

Table C.4 - C.5 lists all capacity data obtained from cycling of cathodes made from lithium manganese oxide ($LiMn_2O_4$)

Table C.4: Capacity values for the three cathode cells with electrode consisting of lithium manganese oxide ($LiMn_2O_4$) + graphene nanopowder (AO-2).

	LMO8 1		LMO8 2		LMO8 3	
Cycle no.	Charge cap. [mAh/g]	Discharge cap. [mAh/g]	Charge cap. [mAh/g]	Discharge cap. [mAh/g]	Charge cap. [mAh/g]	Discharge cap. [mAh/g]
1	106.66	98.19	111.08	101.78	107.36	96.89
2	94.41	91.71	98.32	95.10	90.45	87.39
3	35.83	30.16	39.25	33.72	16.41	13.28
4	31.93	30.94	34.96	33.49	14.73	13.84
5	31.10	30.35	33.49	32.45	14.65	13.98
6	30.22	29.69	32.49	31.84	14.32	13.87
7	29.36	29.00	31.71	31.08	14.15	13.79
8	6.38	5.78	7.38	6.70	0.04	0.01
9	5.71	5.81	6.77	6.86	0.01	0.01
10	5.63	5.78	6.77	6.98	0.01	0.01
11	5.66	5.83	6.79	6.99	0.01	0.01
12	5.69	5.85	6.79	6.98	0.01	0.01
13	0.01	0.00	0.01	0.00	0.00	0.00
14	0.00	0.00	0.00	0.00	0.00	0.00
15	0.00	0.01	0.00	0.00	0.00	0.00
16	0.00	0.01	0.00	0.00	0.00	0.00
17	0.00	0.01	0.00	0.01	0.00	0.00
18	0.00	0.01	0.00	0.00	0.00	0.00
19	0.00	0.01	0.00	0.01	0.00	0.00
20	0.00	0.01	0.00	0.01	0.00	0.00
21	0.00	0.01	0.00	0.01	0.00	0.00
22	0.00	0.01	0.00	0.01	0.00	0.00

Table C.5: Capacity values for the three cathode cells with electrode consisting of lithium manganese oxide ($LiMn_2O_4$) + carbon black (Super P Li).

	LSP8 1		LSP8 2		LSP8 3	
Cycle no.	Charge cap. [mAh/g]	Discharge cap. [mAh/g]	Charge cap. [mAh/g]	Discharge cap. [mAh/g]	Charge cap. [mAh/g]	Discharge cap. [mAh/g]
1	128.07	119.07	142.26	116.95	120.74	114.19
2	121.23	117.82	119.33	115.82	116.21	113.14
3	116.22	113.98	113.50	111.25	110.28	108.12
4	114.78	113.94	111.81	111.03	109.01	108.28
5	114.53	113.73	111.63	110.92	108.87	108.19
6	114.16	113.40	111.33	110.67	108.68	108.03
7	113.89	113.19	110.87	110.18	108.48	107.84
8	106.62	105.47	100.71	99.55	100.41	99.04
9	105.88	105.43	99.93	99.54	99.02	98.70
10	105.53	105.17	99.43	99.14	98.76	98.53
11	105.34	105.00	98.83	98.57	98.87	98.55
12	105.45	105.06	98.69	98.41	98.25	97.98
13	90.58	88.27	74.03	71.37	77.62	74.87
14	88.27	87.95	70.62	70.21	74.48	74.05
15	88.74	88.60	70.63	70.59	75.09	74.96
16	88.57	88.39	70.88	70.90	75.04	74.91
17	88.56	88.44	70.73	70.69	74.36	74.38
18	42.44	40.48	3.09	2.47	7.36	6.78
19	39.68	39.91	1.96	2.16	4.92	5.28
20	40.11	40.32	1.69	1.89	4.51	4.84
21	40.45	40.64	1.59	1.78	4.20	4.50
22	40.01	40.13	1.56	1.73	4.16	4.42

Bibliography

[1] B. Scrosati and J. Garche. Lithium batteries: Status, prospects and future. *Journal of Power Sources*, 195(9):2419–2430, 2010.

[2] G. Kucinskis, G. Bajars, and J. Kleperis. Graphene in lithium ion battery cathode materials: A review. *Journal of Power Sources*, 240:66–79, 2013.

[3] J. M. Tarascon and M. Armand. Issues and challenges facing rechargeable lithium batteries. *Nature*, 414(6861):359–367, 2001.

[4] I. R. M. Kottegoda, Y. Kadoma, H. Ikuta, Y. Uchimoto, and M. Wakihara. High-rate-capable lithium-ion battery based on surface-modified natural graphite anode and substituted spinel cathode for hybrid electric vehicles. *Journal of the Electrochemical Society*, 152(8):A1595–A1599, 2005.

[5] M. Park, X. C. Zhang, M. D. Chung, G. B. Less, and A. M. Sastry. A review of conduction phenomena in Li-ion batteries. *Journal of Power Sources*, 195(24):7904–7929, 2010.

[6] D. Linden and T. B. Reddy. *Handbook of batteries*, pages 1.3–1.10, A5. McGraw-Hill, New York, third edition, 2002.

[7] F. Béguin and E. Frackowiak. *Carbons for Electrochemical Energy Storage and Conversion Systems*. CRC Press, Boca Raton, 2010.

[8] M. S. Dresselhaus and G. Dresselhaus. Intercalation compounds of graphite. *Advances in Physics*, 51(1):1–186, 2002.

[9] A. Manthiram and T. Muraliganth. *Lithium Intercalation Cathode Materials for Lithium-Ion Batteries*, pages 341–375. Wiley-VCH Verlag GmbH & Co. KGaA, 2011.

[10] P. H. D. Tran. Structural and electrochemical characterization of graphite materials for Li-ion batteries. Master's thesis, Norwegian University of Science and Technology, Department of Materials Science and Engineering, 2012.

[11] A Guide to Understanding Battery Specifications. `http://web.mit.edu/evt/summary_battery_specifications.pdf`. Accessed: 2014-05-25.

[12] P. Ramadass, B. Haran, R. White, and B. N. Popov. Capacity fade of Sony 18650 cells cycled at elevated temperatures Part I. Cycling performance. *Journal of Power Sources*, 112(2):606–613, 2002.

[13] K. Xu. Electrolytes and Interphasial Chemistry in Li Ion Devices. *Energies*, 3(1):135–154, 2010.

[14] E. Antolini. $LiCoO_2$: formation, structure, lithium and oxygen nonstoichiometry, electrochemical behaviour and transport properties. *Solid State Ionics*, 170(3-4):159–171, 2004.

[15] J. W. Fergus. Recent developments in cathode materials for lithium ion batteries. *Journal of Power Sources*, 195(4):939–954, 2010.

[16] M. K. Aydinol and G. Ceder. First-Principles Prediction of Insertion Potentials in Li-Mn Oxides for Secondary Li Batteries. *Journal of The Electrochemical Society*, 144(11):3832–3835, 1997.

[17] J. Tu *et al.* Enhanced low voltage cycling stability of $LiMn_2O_4$ cathode by ZnO coating for lithium ion batteries. *Journal of Alloys and Compounds*, 432(1–2):313–317, 2007.

[18] Y.-H. Chen *et al.* Selection of Conductive Additives in Li-Ion Battery Cathodes: A Numerical Study. *Journal of The Electrochemical Society*, 154(10):A978–A986, 2007.

[19] H. Zheng *et al.* Cooperation between Active Material, Polymeric Binder and Conductive Carbon Additive in Lithium Ion Battery Cathode. *The Journal of Physical Chemistry C*, 116(7):4875–4882, 2012.

[20] J. K. Hong, J. H. Lee, and S. M. Oh. Effect of carbon additive on electrochemical performance of $LiCoO_2$ composite cathodes. *Journal of Power Sources*, 111(1):90–96, 2002.

[21] K. Xu. Nonaqueous liquid electrolytes for lithium-based rechargeable batteries. *Chemical Reviews*, 104(10):4303–4417, 2004.

[22] Ø. Gullbrekken. Thermal characterisation of anode materials for Li-ion batteries. Master's thesis, Norwegian University of Science and Technology, Department of Materials Science and Engineering, 2012.

[23] S. S. Zhang. A review on electrolyte additives for lithium-ion batteries. *Journal of Power Sources*, 162(2):1379–1394, 2006.

[24] A. M. Andersson and K. Edstrom. Chemical composition and morphology of the elevated temperature sei on graphite. *Journal of the Electrochemical Society*, 148(10):A1100–A1109, 2001.

[25] Z. H. Chen and K. Amine. Tris(pentafluorophenyl) borane as an additive to improve the power capabilities of lithium-ion batteries. *Journal of the Electrochemical Society*, 153(6):A1221–A1225, 2006.

[26] X. H. Sun, H. S. Lee, X. Q. Yang, and J. McBreen. The compatibility of a boron-based anion receptor with the carbon anode in lithium-ion batteries. *Electrochemical and Solid State Letters*, 6(2):A43–A46, 2003.

[27] L. F. Li *et al.* New electrolytes for lithium ion batteries using LiF salt and boron based anion receptors. *Journal of Power Sources*, 184(2):517–521, 2008.

[28] D. Goers, H. Buqa, L. Hardwick, A. Würsig, and P. Novák. Raman spectroscopic and structural studies of heat-treated graphites for lithium-ion batteries. *Ionics*, 9(3-4):258–265, 2003.

[29] K. Kinoshita. *Carbons*, pages 269–284. Wiley-VCH Verlag GmbH & Co. KGaA, 2011.

[30] T. Ohzuku, Y. Iwakoshi, and K. Sawai. Formation of Lithium-Graphite Intercalation Compounds in Nonaqueous Electrolytes and Their Application as a Negative Electrode for a Lithium Ion (Shuttlecock) Cell. *Journal of The Electrochemical Society*, 140(9):2490–2498, 1993.

[31] G. Aylward and T. Findlay. *SI Chemical Data*. John Wiley & Sons, Australia, 6th edition, 2008.

[32] E. Peled. The electrochemical-behavior of alkali and alkaline-earth metals in non-aqueous battery systems - the solid electrolyte interphase model. *Journal of the Electrochemical Society*, 126(12):2047–2051, 1979.

[33] C. Yuqin, L. Hong, W. Lie, and L. Tianhong. Irreversible capacity loss of graphite electrode in lithium-ion batteries. *Journal of Power Sources*, 68(2):187–190, 1997.

[34] D. Aurbach and Y. Gofer. The Behavior of Lithium Electrodes in Mixtures of Alkyl Carbonates and Ethers. *Journal of The Electrochemical Society*, 138(12):3529–3536, 1991.

[35] L. H. Huang, Z. H. Min, and Q. Y. Zhang. Solid electrolyte inter-phase on graphite anodes in Li-ion batteries. *Reviews on Advanced Materials Science*, 36(1):13–20, 2014.

[36] C. E. L. Foss. *Thermal Stability and Electrochemical Performance of Graphite Anodes in Li-ion Batteries*. PhD thesis, Norwegian University of Science and Technology, Department of Materials Science and Engineering, 2014.

[37] P. Verma, P. Maire, and P. Novák. A review of the features and analyses of the solid electrolyte interphase in Li-ion batteries. *Electrochimica Acta*, 55(22):6332–6341, 2010.

[38] A. M. Andersson, A. Henningson, H. Siegbahn, U. Jansson, and K. Edstrom. Electrochemically lithiated graphite characterised by photoelectron spectroscopy. *Journal of Power Sources*, 119:522–527, 2003.

[39] K. Edstrom, M. Herstedt, and D. P. Abraham. A new look at the solid electrolyte interphase on graphite anodes in Li-ion batteries. *Journal of Power Sources*, 153(2):380–384, 2006.

[40] S. S. Zhang. A review on electrolyte additives for lithium-ion batteries. *Journal of Power Sources*, 162(2):1379–1394, 2006.

[41] D. Aurbach, M. D. Levi, E. Levi, and A. Schechter. Failure and stabilization mechanisms of graphite electrodes. *Journal of Physical Chemistry B*, 101(12):2195–2206, 1997.

[42] E. Peled *et al.* Composition, depth profiles and lateral distribution of materials in the SEI built on HOPG-TOF SIMS and XPS studies. *Journal of Power Sources*, 97-8:52–57, 2001.

[43] H. C. Wu, H. C. Wu, E. Lee, and N. L. Wu. High-temperature carbon-coated aluminum current collector for enhanced power performance of $LiFePO_4$ electrode of Li-ion batteries. *Electrochemistry Communications*, 12(3):488–491, 2010.

[44] T. Abe, H. Fukuda, Y. Iriyama, and Z. Ogumi. Solvated Li-ion transfer at interface between graphite and electrolyte. *Journal of the Electrochemical Society*, 151(8):A1120–A1123, 2004.

[45] H. C. Wu, E. Lee, N. L. Wu, and T. R. Jow. Effects of current collectors on power performance of $Li_4Ti_5O_{12}$ anode for Li-ion battery. *Journal of Power Sources*, 197:301–304, 2012.

[46] P. V. Braun, J. Cho, J. H. Pikul, W. P. King, and H. Zhang. High power rechargeable batteries. *Current Opinion in Solid State and Materials Science*, 16(4):186–198, 2012.

[47] H. Buqa, D. Goers, M. Holzapfel, M. E. Spahr, and P. Novák. High Rate Capability of Graphite Negative Electrodes for Lithium-Ion Batteries. *Journal of The Electrochemical Society*, 152(2):A474–A481, 2005.

[48] F. A. Miller and G. B. Kauffman. C. V. Raman and the discovery of the Raman effect. *Journal of Chemical Education*, 66(10):795, 1989.

[49] D. D. L. Chung. Review Graphite. *Journal of materials science*, 37(8):1475–1489, 2002.

[50] Raman Spectroscopy of Graphite. `http://www.jumwalter.de/raman.htm`. Accessed: 2014-05-16.

[51] F. Tuinstra and J. L. Koenig. Raman Spectrum of Graphite. *The Journal of Chemical Physics*, 53(3):1126–1130, 1970.

[52] V. Zólyomi, J. Koltai, and J. Kürti. Resonance Raman spectroscopy of graphite and graphene. *physica status solidi (b)*, 248(11):2435–2444, 2011.

[53] Y. W. Zhu *et al.* Graphene and Graphene Oxide: Synthesis, Properties, and Applications. *Advanced Materials*, 22(35):3906–3924, 2010.

[54] Geochemical Instrumentation and Analysis. `http://serc.carleton.edu/research$_$education/geochemsheets/techniques/SEM.html`. Accessed: 2014-05-16.

[55] Signals in Scanning Electron Microscopy. `http://www.microscopy.ethz.ch/sem$_$\detectors.htm`. Accessed: 2014-05-16.

[56] `http://ipn2.epfl.ch/CHBU/images/cvd.gif`. Accessed: 2014-05-19.

[57] The Power of Synergies. `http://www.timcal.com/scopi/group/timcal/timcal.nsf/pagesref/MCOA-7S6K2K/$\protect\T1\textdollar$File/Brochure$_$$Carbon$_$Powders$_$for$_$Lithium$_$Battery$_$Systems.pdf`. Accessed: 2014-05-19.

[58] Graphene Nanopowder 8 nm Flakes - 25g. `https://graphene-supermarket.com/`

Graphene-Nanopowder-8-nm-Flakes-25-g.html. Accessed: 2014-05-19.

[59] Lithium manganese oxide. http://www.sigmaaldrich.com/catalog/product/aldrich/\725129?lang=en$&$region=NO. Accessed: 2014-05-19.

[60] T. Eriksson. *$LiMn_2O_4$ as a Li-ion Battery Cathode. From Bulk to Electrolyte Interface*. PhD thesis, Uppsala University, Department of Materials Chemistry, 2001.